The ground deformation of the south-eastern flank of Mount Etna monitored by GNSS and SAR interferometry from 2016 to 2019

Francesco Carnemolla, Giorgio de Guidi, Alessandro Bonforte, Fabio Brighenti, Pierre Briole

Geophysical Journal International

Geophys. J. Int. (2023) **234,** 664–682
Advance Access publication 2023 February 25
GJI Geodynamics and Tectonics

https://doi.org/10.1093/gji/ggad088

The ground deformation of the south-eastern flank of Mount Etna monitored by GNSS and SAR interferometry from 2016 to 2019

Francesco Carnemolla [1], Giorgio De Guidi [1,2], Alessandro Bonforte [3], Fabio Brighenti [1] and Pierre Briole [3,4]

[1] *Dipartimento di Scienze Biologiche, Geologiche e Ambientali, University of Catania, Corso Italia, 57, 95129, Catania E-mail: francesco.carnemolla@unict.it*
[2] *CRUST – Centro inteRUniversitario per l'analisi SismoTettonica tridimensionale con applicazioni territoriali,Via dei Vestini, 31, 66100, Chieti, Italy*
[3] *Istituto Nazionale di Geofisica e Vulcanologia, Osservatorio Etneo,, Piazza Roma* 2, 95125 *Catania, Italy*
[4] *Laboratoire de Géologie de l'École Normale Supérieure, , UMR CNRS-ENS-PSL* 8538, 24 *Rue Lhomond,* 75005 *Paris, France*

Accepted 2023 February 23. Received 2023 January 29; in original form 2022 July 13

SUMMARY

The south-eastern sector of the Mount Etna, Italy, is characterized by numerous active faults, in particular the Belpasso–Ognina lineament, the Tremestieri–San Gregorio–Acitrezza fault, the Trecastagni fault and the Fiandaca–Nizzeti fault including the Timpe Fault System. Their activity is the result of both volcanism and tectonics. Here, we analyse the ground deformation occurred from 2016 to 2019 across those active faults by using the GNSS data acquired at 22 permanent stations and 35 campaign points observed by the Etna Observatory (INGV) and by the University of Catania. We also use the time-series of line of sight displacement of permanent scatterers SENTINEL-1 A-DInSAR obtained by using the P-SBAS tool of the ESA GEP-TEP (Geohazards Thematic Exploitation Platform) service. We discriminate the contributions of the regional tectonic strain, the inflations, the deflations of the volcano and the gravitational sliding in order to analyse the deformation along the faults of the south-eastern flank of Etna. The shallow and destructive $M_w = 4.9$ earthquake of 2018 December 26 occurred within the studied area two days after a dyke intrusion, that propagated beneath the centre of the volcano accompanied by a short eruption. Both GNSS and InSAR time-series document well those events and allow to investigate the post-seismic sliding across the faults of south-eastern flank. We analyse the slow slip events (SSE) that are observed in the GNSS and InSAR time-series in the vicinity of the Acitrezza fault. We quantify and discuss the tectonic origin of the Belpasso–Ognina lineament that we interpreted as a tear fault.

Key words: Satellite geodesy; Transient deformation; Interferometry; Fractures, fault, and high strain deformation zone; Volcano monitoring; Etna.

1 INTRODUCTION

Mount Etna, Italy, is one of the most active volcanoes in the world and one of the most studied since ancient time. It is located in eastern Sicily, in the collision zone between the Eurasian and Nubian plates. The area is characterized by NNW-SSE compression and WNW-ESE extension (Fig. 1) which has been studied by many authors (Bousquet & Lanzafame 1986; Westaway 1993; Tortorici *et al.* 1995; Firth *et al.* 1996; Hirn *et al.* 1997; Stewart *et al.* 1997; Kershaw 2000; Monaco & Tortorici 2000; Rust & Kershaw 2000; Antonioli *et al.* 2003; De Guidi *et al.* 2003; D'Agostino & Selvaggi 2004; Goes *et al.* 2004; D'Agostino *et al.* 2008; Schellart 2010; Faccenna *et al.* 2011; Palano *et al.* 2012; Spampinato *et al.* 2012; Ristuccia *et al.* 2013).

On the volcano, the tectonics strain also includes the effect of dyke injections, extensional fractures, shallow faulting induced by the volcanic activity and the gravitational loading of the topography (Poland *et al.* 2017). These phenomena cause the eastern flank of the volcano to slip eastwards. According to De Guidi *et al.* (2018, and reference therein), three main fault systems delineate this unstable eastern flank: the Pernicana Fault to the northeast, the Timpe

Fault system to the east and the South Fault system to the southeast (Fig. 1).

A number of faults are involved in the overall deformation of the Etna's south-eastern flank (Fig. 1): the Belpasso–Ognina lineament (BOL), Tremestieri (TMF), San Gregorio-Acitrezza (SGAF), Trecastagni (TF), Nizzeti (NF), Fiandaca (FF) and Acireale (AF) faults. Although the Belpasso–Ognina lineament has no morphological signature, InSAR, CO_2 and Rn evidence its activity (Bonforte *et al.* 2013). To the south, the Tremestieri fault and the San Gregorio–Acitrezza fault form a unique system that accommodates most of deformation of the eastern flank. The former is characterized by a right lateral transtensive kinematic. The latter is characterized by creep deformation with a right-lateral component, and exhibits ground fractures and blind lineaments detected by InSAR (Froger *et al.* 2001; Solaro *et al.* 2010; Bonforte *et al.* 2011). It has been monitored since 2014 by a dense GNSS network (De Guidi *et al.* 2018) tailored to sample the geological structures analysed by Imposa *et al.* (2015).

The Trecastagni fault extends with NNW-SSE direction until it joins the San Gregorio–Acitrezza fault. It is a normal fault that has produced a 10 m hight scarp. The NNW-SSE striking Nizzeti fault is characterized by a linear scarp up to 100 m high. To the north it joins the southern end of the NNW-SSE trending Fiandaca fault, which is a normal fault with an oblique-dextral component. The Acireale fault has scarps ranging from 10 to 100 m high. Varius vertical slip rates for this fault have been estimated by different authors: 1.1 and 1.9 mm yr^{-1} according to Monaco *et al.* (1997), $\sim$ 4.3 mm yr^{-1}, according to Azzaro *et al.* (2012) and 3 mm yr^{-1} according to Branca *et al.* (2014).

South of the eastern flank, are the Terreforti and Catania anticlines (Labaume *et al.* 1990; Catalano *et al.* 2011; Ristuccia *et al.* 2013; De Guidi *et al.* 2015). Using morphological, seismological and geodetic data, Palano *et al.* (2012) and De Guidi *et al.* (2015) estimated an uplift of 10 mm yr^{-1} and a shortening of 5 mm yr^{-1} for these anticlines, consistent with the activity of a putative low-angle blind thrust. Froger *et al.* (2001) measured a strain rate of 12 mm yr^{-1} in the ascending ERS InSAR LOS direction across these anticlines. Bonforte *et al.* (2011) measured an uplift rate of nearly 10 mm yr^{-1}, while Borgia *et al.* (2000) give an absolute uplift rate of 15–20 mm yr^{-1} and a shortening of 12 mm yr^{-1}. Borgia *et al.* (2000) interpreted this basal deformation as a gravitational effect of the volcanic loading, while Palano *et al.* (2012) interpreted it as a thrust propagation fold at the front of the chain. Solaro *et al.* (2010) measured vertical uplift of $\sim$ 6 mm yr^{-1} associated with the development of a fault-propagation fold independent of volcanism.

The moderate seismicity compared to the strain intensity suggests that most of the strain occurring on the south-eastern flank of Etna is not seismically accommodated. Creeping faults are observed in several places, see for example, Lo Giudice & Rasà (1992) and Rasà *et al.* (1996). In addition, since mid-2008, GNSS stations located on the lower south-eastern flank have episodically recorded significant strain transients. There is no unique interpretation in the literature of those slip transient, called slow slip events (SSEs, Mattia *et al.* 2015; Palano 2016; Bruno *et al.* 2017; Palano *et al.* 2022).

Strain transients on the eastern flank of the volcano are often correlated with lateral and summit eruptions and can occur years after these eruption (Bonaccorso *et al.* 2006; Alparone *et al.* 2011). For example, two days after the dyke intrusion and eruption of 2018 December 24, an $M_w = 4.9$ earthquake struck the lower SE flank of the volcano, activating the Fiandaca fault (Bonforte *et al.* 2019; Mattia *et al.* 2020; Monaco *et al.* 2021; De Novellis *et al.* 2019).

In the following sections we jointly analyse GNSS and InSAR data to document this deformation in the period 2016–2019.

2 GNSS DATA

2.1 Permanent GNSS data

We analysed the data collected by twenty-two GNSS stations (Table 1) belonging to the national RING array (INGV RING Working Group, 2016; http://ring.gm.ingv.it/) and the local INGV-OE array (Bonforte *et al.* 2016). Eight of them are located outside the volcanic. We processed the data with the GipsyX-1.3 software (https://gipsy-oasis.jpl.nasa.gov) distributed by the Jet Propulsion Laboratory (Bertiger *et al.* 2020), using precise orbits and clock parameters, absolute IGS antenna phase centres and Global Mapping Functions (Boehm *et al.* 2006) for the troposphere. Table 1 shows the velocities of the stations in the International Terrestrial Reference Frame 2014 (ITRF2014, Altamimi *et al.* 2016). The average ITRF2014 velocity of the eight stations outside Etna is $V_E = 21.4 \pm 0.3$ mm yr^{-1} and $V_N = 19.4 \pm 0.3$ mm yr^{-1} (Carnemolla 2021). In the following, this average regional velocity of eastern Sicily is subtracted to analyse the local deformation of the volcano. Figs 2(b) and (c) show the residual velocities obtained after this subtraction. Those residual velocities, due to local volcanic and tectonic processes, are discussed below.

2.2 Campaign GNSS data

The permanent stations and the campaign points are shown in Fig. 3. The density of the permanent stations is not sufficient to document the activity of the different faults one by one. Therefore, over the last three decades, additional campaign points have been progressively installed gradually and periodically monitored. Here, we have calculated the data of 35 campaign points (Table 2), 7 of which have been monitored annually by INGV-OE since the late-1990s (Bonforte *et al.* 2016, see Supporting Information S1) and 28 observed by the University of Catania since 2014 or later (De Guidi *et al.* 2018; Carnemolla 2021, see Supporting Information S2).

The velocity fields of the San Gregorio and Acitrezza networks are shown in Figs 3(b) and (c). The velocities are referred to the Eastern Sicily reference frame and locally also to the 02SG reference frame (Carnemolla 2021). In the first case, the velocities still represent the global deformation of Etna, while in the second case they represent the differential motion of the two blocks separated by the San Gregorio–Acitrezza fault. In this local reference frame, the northern block is moving eastwards with respect to the southern block, and the eastward velocity increases along the fault toward the east To the south, considering the short time span sampled by the campaign GNSS observations, we estimate a differential eastward velocity between the two blocks separated by the Belpasso–Ognina lineament of $\sim$ 5 mm yr^{-1} with a relative left component.

The points velocities are also clearly influenced by transient deformation during the post-seismic period following the 2018 December 26 earthquake.

3 SAR INTERFEROMETRY

The online Geohazards Thematic Exploitation Platform (GEP-TEP, ESA 2015) was used for the interferometric analysis, in particular the P-SBAS Sentinel-1 processing on-demand module (Casu *et al.* 2014; de Luca *et al.* 2015; Manunta *et al.* 2019). This module

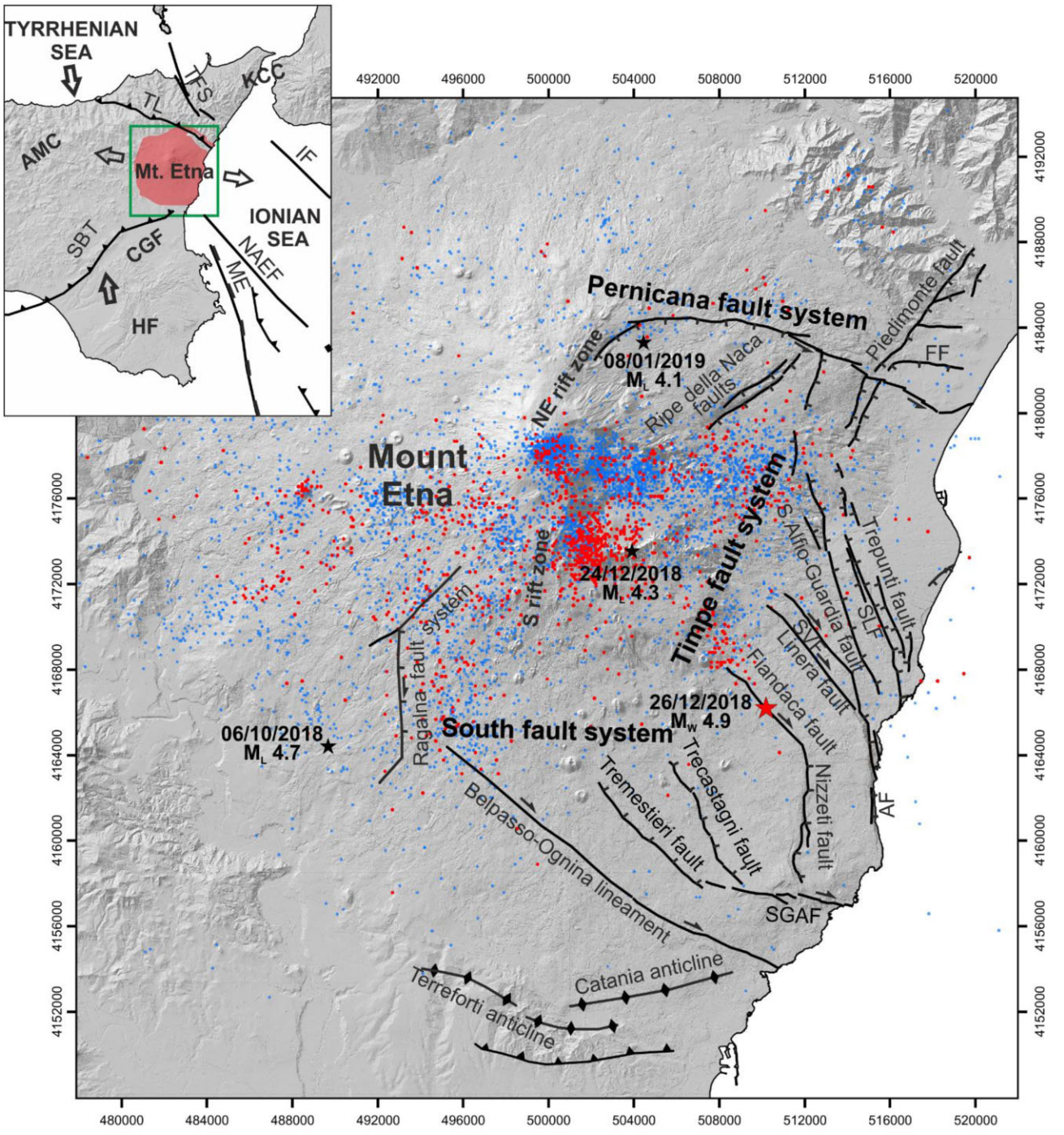

Figure 1. Map of Mount Etna with the main volcano-tectonic elements. On the top left, location of the volcano and the main tectonic structures of eastern Sicily; Appenninic–Maghrebian chain, AMC, Kabilo Calabride chain, KCC, Hyblean foreland, HF, Catania–Gela foredeep, CGF, Sicilia Basal thrust, SBT, Taormina line, TL, Tindari fault system, TFS, Ionian fault, IF, North Alfeo Etna fault, NAEF and Malta escarpment, ME. The major fault zones are plotted. SGAF, San Gregorio Acitrezza Fault; AF, Acireale Fault; SVF, Santa Venerina Fault; SLF, San Leonardello Fault and FF, Fiumefreddo Fault. Blue points are the earthquakes occurred during the 2016–2019 period with $M_L > 1$. Red points are the earthquakes occurred during from the 2018 December 1 and 2019 January 31 with $M_L > 1$. Major shock ($M_L > 4$) occurred during the 2016–2019 are represented with black stars. Red star is the $M_w = 4.9$ earthquake of 2018 December 26. The seismicity was extract from Mt. Etna Seismic Catalog (http://sismoweb.ct.ingv.it/, Alparone *et al.* 2022). The 2016–2019 seismicity is provided as Supporting Information 6. Shaded relief is carried out from the *Digital Terrain Model* (2 m resolution) derived from a LIDAR acquired by the Regione Siciliana *(*Regione Siciliana 2010*)*.

uses the Parallel SBAS Interferometry Chain algorithm proposed by Berardino *et al.* (2002) and Casu *et al.* (2014). The data set contains 309 IW Sentinel 1 SLC SAR data from both the ascending track 44 and the descending track 124. The digital elevation model (DEM) used to remove the topography phase components is the 1 arcsec Shuttle Radar Topography Mission (SRTM) DEM. The number of look azimuth direction and range direction are 5 and 20 respectively. The pixel resolution is 1 arcsec. A Goldstein spatial

Table 1: Velocities of permanent GNSS stations in the ITRF2014 (Altamimi *et al.* 2016). Fourteen stations belong to the INGV-OE array deployed around Mount Etna, seven belong to the national array RING, and one to the IGS and EUREF networks.

Code	Name	Operator	Long.	Lat.	V_E	V_N	σ_E	σ_N
			°		mm yr^{-1}			
EBAG	Baglio	INGV-OE	15.161	37.702	31.9	6.1	1.8	1.1
EBDA	Bosco di Aci	INGV-OE	15.122	37.634	31.8	10.4	1.9	1.9
EC10		INGV-OE	15.083	37.692	32.2	5.2	0.6	0.6
EIIV	Catania	INGV-OE	15.082	37.514	22.6	17.6	0.4	0.4
ELAC	Isola Lachea	INGV-OE	15.166	37.561	30.6	14.3	1.0	0.8
ELEO	San Leonardello	INGV-OE	15.172	37.692	61.7	-1.2	2.	2.
ELIN	Linera	INGV-OE	15.136	37.667	33.1	7.1	1.4	1.5
EMFN	Monte Fontane	INGV-OE	15.090	37.736	39.7	3.5	2.1	2.4
ENIC	Nicolosi	INGV-OE	15.019	37.614	26.3	7.6	0.5	1.1
EPED	Pedara	INGV-OE	15.06	37.617	28	11	1.2	1.2
EPOZ	Pozzillo	INGV-OE	15.189	37.672	39.7	8.9	1.2	0.7
ERIP	Riposto	INGV-OE	15.197	37.729	32.1	12.4	1.6	1.1
ESPC	Serra Pizzuta C.	INGV-OE	15.027	37.693	30.7	9.7	0.8	1.2
ETEC	Santa Tecla	INGV-OE	15.178	37.638	37.6	13.1	1.3	0.9
GALF	Gagliano	RING	14.567	37.711	21.3	19.0	0.5	0.5
HAGA	Brucoli	RING	15.155	37.286	21.9	19.5	0.4	0.4
HAV1	Avola	RING	15.122	36.960	21.5	19.8	0.5	0.4
HLNI	Scordia	RING	14.872	37.349	21.5	19.1	0.5	0.5
HMDC	Ragusa	RING	14.783	36.959	21.2	19.4	0.5	0.5
MNOV	Novara di Sicilia	RING	15.136	38.029	20.8	19.6	0.5	0.6
NOT1	Noto	IGS & EUREF	14.99	36.876	21.2	19.5	0.5	0.5
SSYX	Sortino	RING	15.076	37.158	21.6	19.6	0.4	0.4

filter (Goldstein & Werner 1998) with a value of 0.5 was applied. The P-SBAS Sentinel-1 processing on-demand module uses the noise filtering procedure proposed by Pepe *et al.* (2015), which is based on the pixel-by-pixel solution of a nonlinear minimization problem (Manunta *et al.* 2019). The phase unwrapping was performed using the advanced EMCF algorithm (Pepe *et al.* 2015). The advanced EMCF algorithm is applied to pixels with a triangular coherence greater than a fixed threshold (set to 0.85 in this analysis). The main drawback of this web tool is that the users cannot modify many processing parameters and cannot include a tectonic model, but it provides a great opportunity for the scientific community to obtain the interferometric data.

828 interferograms were produced with perpendicular baselines ranging between −95 and 104 m and a maximum temporal separation of 170 d.

The displacements rates for 2016, 2017, 2018 and 2019 have been calculated using as a reference point the coherent pixel closest to the EIIV GNSS station , located on the roof of the headquarters of the Istituto Nazionale di Geofisica e Vulcanologia (INGV) in Catania. The GNSS displacements at EIIV are used to determine the displacement of EIIV along the line of sight (LOS) of the ascending and descending Sentinel-1 images. Then, the LOS-projected times series of EIIV are subtracted. Thus, the displacements of all pixels in the images are referred to EIIV.

When calculating the annual PS time-series, we aligned them with the GNSS time-series by applying a constant correction for each year from 2016 to 2019. This phase shift was calculated by comparing the LOS-projected GNSS time-series with the PS surrounding the GNSS stations (EBDA, ELAC, ENIC, EPED and ETEC, Fig. 4). There is a good agreement between the GNSS and PS time-series, except at the easternmost stations ETEC, EBDA and ELAC which have root mean square scatter greater than 6.5 mm yr^{-1} (Fig. 4).

We then converted the LOS velocity to the East and Up component, assuming that the contribution of the North velocity has a small influence on the LOS velocity. This is a valid assumption given the azimuth of the GNSS velocities. The comparison between GNSS and PS show that the correction is not uniform over the whole south-eastern flank, but varies between the lower and middle flank of the volcano. Here we only consider the relative motion between the hangingwall and footwall of the faults, so the biases due to the conversion to the east and up component can be neglected (Carnemolla 2021).

4 OFFSETS ACROSS FOUR MAJOR FAULTS

The permanent scatterers, located less than 500 m from either side of the faults, were selected to estimate the fault offsets and to calculate the slip rate along the fault. Four faults are analysed: (i) the Belpasso–Ognina lineament, (ii) the Tremestieri–San Gregorio–Acitrezza fault, (iii) the Trecastagni fault and (iv) the Fiandaca–Nizzeti fault.

For each fault segment, two profiles were created according to the direction of these faults, using the method developed by De Michele & Briole (2007). Each profile is analysed for each years from 2016 to 2019 (see Supporting Information S3), so eight profiles are calculated, two for each fault (Fig. 5).

4.1 The Fiandaca and Nizzeti fault

Following the dyke intrusion of 2018 December 24, the $M_w = 4.9$ earthquake of 2018 December 26 activated the Fiandaca fault along its entire length (Fig. 6). It generated ground fractures that continued to open as a post-seismic deformation a month after the earthquake (Tringali *et al.* 2022). In 2019, this fault shows the highest displacements recorded in the last four years in both the eastern and vertical components. Considering the eastern component, the Fiandaca–Nizzeti fault shows an offset between 20 and 50 mm yr^{-1}. The offset is maximum on the northern part of the

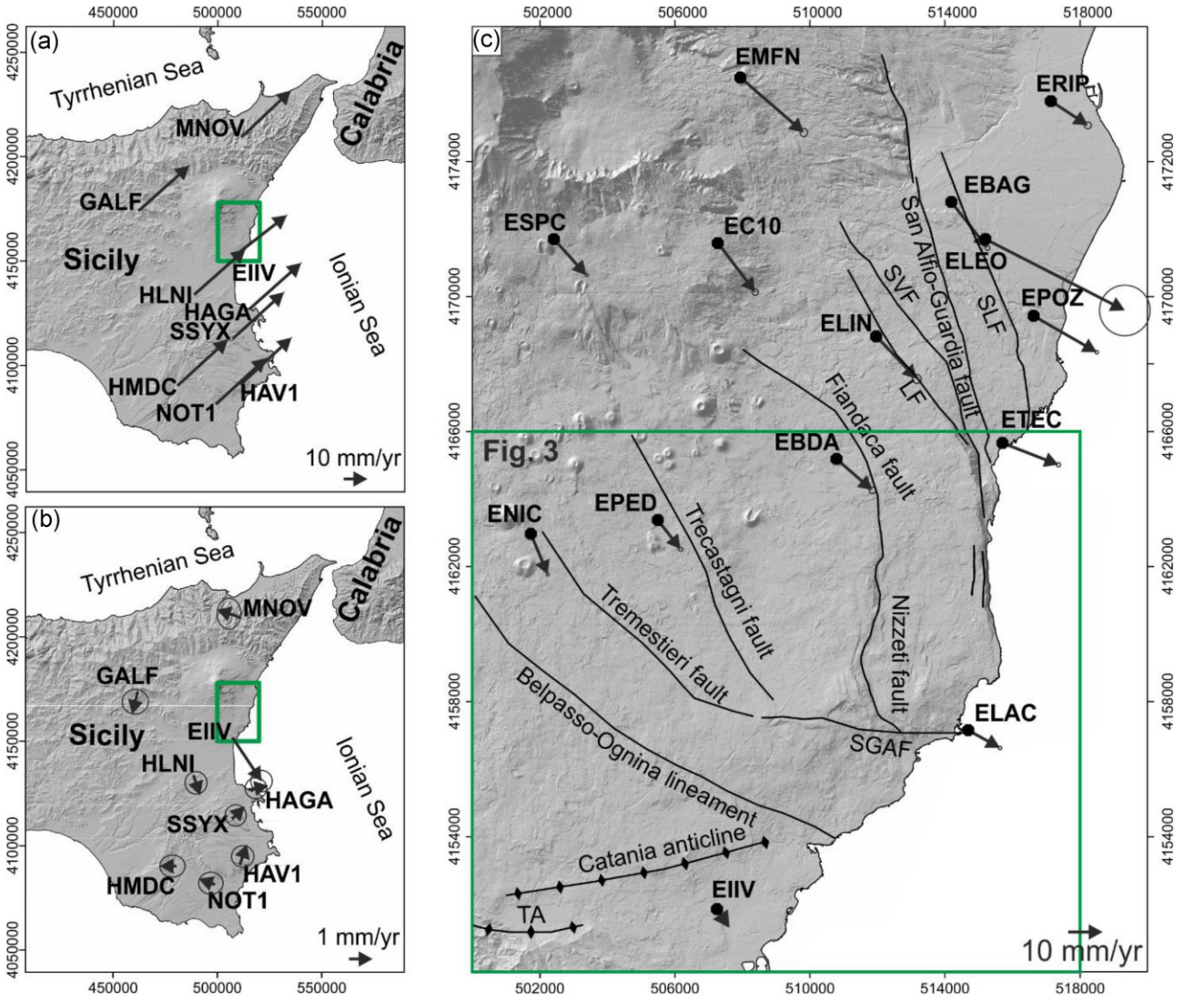

Figure 2. (a) On the left velocity fields of eastern Sicily in ITRF14 reference frame and (b) residual velocity considering the southeastern Sicily stable. (c) Velocity field of the eastern flank of Mount Etna determined by GNSS permanent stations belonging to the INGV-OE; TA Terreforti Anticline.

profile, corresponding to the Fiandaca fault, and then decreases towards the south to 20–30 mm yr^{-1} on the Nizzeti fault (Fig. 7). The vertical component shows a subsidence of about 40–50 mm yr^{-1} in the hangingwall block, while there is no corresponding uplift in the footwall block. This implies that the motion is not the response of an elastic medium to a dislocation. We believe that it is dominated by gravitational slip of the eastern flank of the volcano.

In 2016, the Nizzeti fault shows a constant displacement of ∼10 mm yr^{-1} only in its southern part at the junction with the San Gregorio–Acitrezza fault (see Supporting Information S3).

4.2 The Trecastagni fault and Tremestieri–San Gregorio–Acitrezza fault system

According to Bonforte *et al.* (2013) the Trecastagni fault accommodates a slip 5 mm yr^{-1} between the two adjacent blocks and it shows a dominant vertical slip, with a downthrown of the hangingwall (on the eastern side) at a rate of ∼ 4 mm yr^{-1} up to 6–7 mm yr^{-1} 1 km away from this fault on the hangingwall. Here, we observed that this fault shows a vertical displacement on the hangingwall of ∼5 mm yr^{-1} in 2016 and 2018, increasing to 17 mm yr^{-1} in 2019. Horizontal slip is ∼10 mm yr^{-1} over its entire length in 2016 and 2 mm yr^{-1} on 2018.

According to Froger *et al.* (2001) and Solaro *et al.* (2010), the Tremestieri fault has a slip rate of 5–6 mm yr^{-1}. The vertical component of the relative motion decreases progressively along the fault from 4 mm yr^{-1} in the western part to 0 mm yr^{-1} in the eastern part. From 2016 to 2018, we observe that this fault does not show a clear offset in the PS data, except in 2019, which is 3 mm yr^{-1} for the eastern component and 8 mm yr^{-1} for the vertical component.

On average from 2016 to 2019, the Trecastagni fault is more active in 2016, 2018 and 2019. In 2019 it is influenced by the events of 2018, while the Tremestieri Fault does not seem to be involved in this process. Using InSAR observations, Solaro *et al.* (2010) have already shown that these two structures have variable slip rate. For example, in the early 2000s, the Tremestieri fault accommodated more deformation of the eastern flank more than Trecastagni fault, while from 2016, the later accommodates most of the deformation. Analysing the vertical component, no corresponding uplift is observed in the footwalls of the faults.

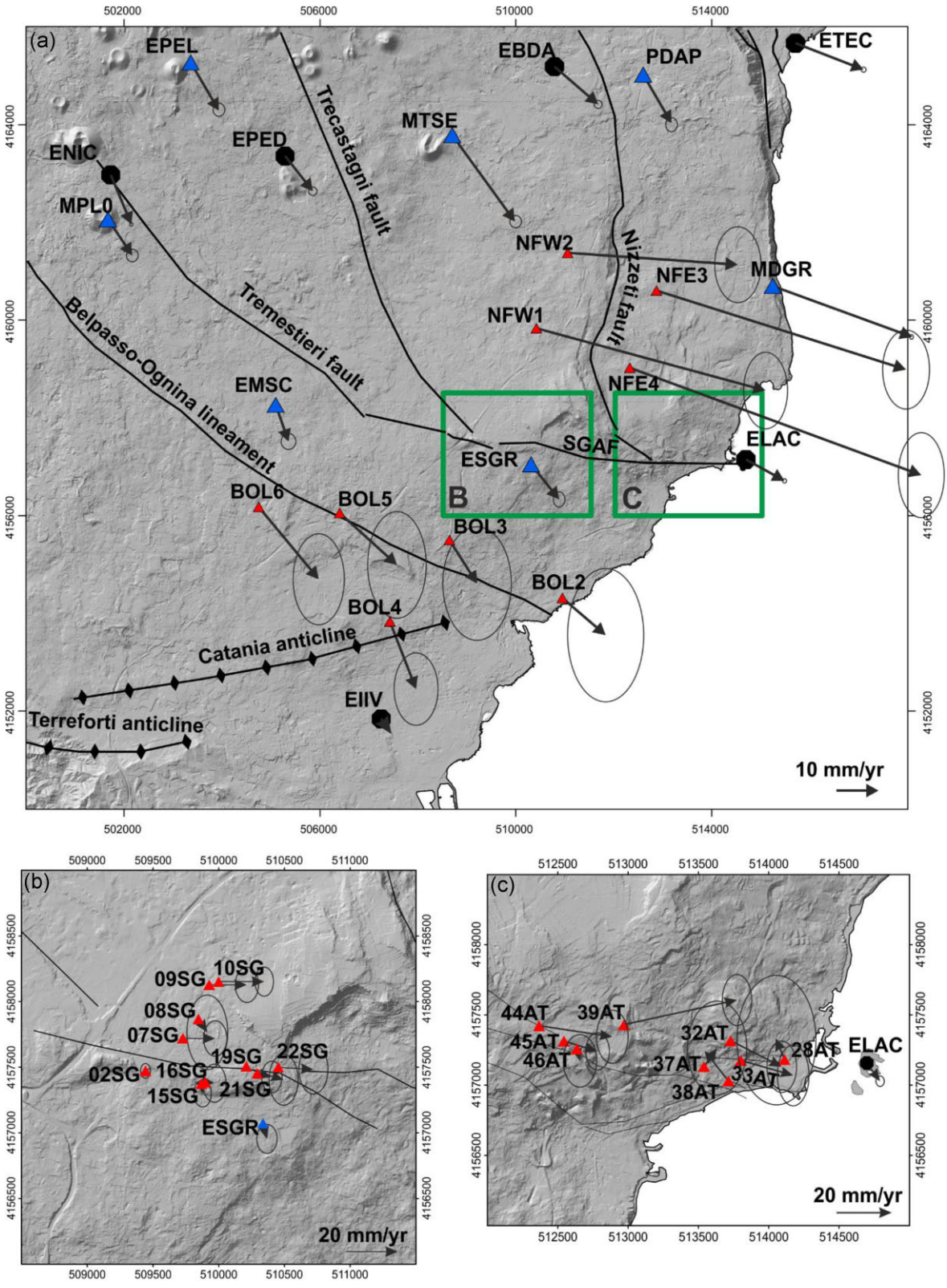

Figure 3. (a) Velocity fields of the south-eastern flank of Mount Etna considering the eastern Sicily stable. The GNSS permanent stations and campaign points belonging to the INGV-OE are in black. Red triangles are the GNSS campaign stations belonging to the UNICT-Net. (b) Velocity field of San Gregorio and (c) velocity field of Acitrezza referred to the 02SG reference frame.

Table 2: Velocities of campaign GNSS stations in the ITRF2014.

Code	Period of operation	Operator	Long. °	Lat.	V_E mm yr^{-1}	V_N	σ_E	σ_N
EMSC	2007–2019	INGV-OE	15.058	37.571	24.42	10.68	0.06	0.10
EPEL	2005–2019	INGV-OE	15.038	37.635	28.13	7.84	0.05	0.09
ESGR	2012–2019	INGV-OE	15.117	37.560	28.09	11.02	0.15	0.28
MDGR	1997–2019	INGV-OE	15.173	37.593	54.60	7.26	0.13	0.24
MPL0	1994–2007	INGV-OE	15.019	37.606	27.20	10.73	0.15	0.18
PDAP	2001–2019	INGV-OE	15.143	37.632	44.48	2.05	0.10	0.18
MTSE	1997–2005	INGV-OE	15.099	37.621	36.30	−1.17	0.39	0.41
02SG	2015–2020	UC San Gregorio net	15.107	37.564	29.7	5.0	1.4	2.2
07SG	2015–2020	UC San Gregorio net	15.110	37.566	42.2	5.1	2.2	3.4
08SG	2015–2017	UC San Gregorio net	15.111	37.568	33.2	10.3	4.0	7.2
09SG	2015–2020	UC San Gregorio net	15.112	37.570	44.3	4.9	2.2	3.8
10SG	2015–2020	UC San Gregorio net	15.113	37.570	47.4	5.0	1.7	2.8
15SG	2015–2020	UC San Gregorio net	15.112	37.563	30.3	8.8	1.7	2.8
16SG	2015–2019	UC San Gregorio net	15.112	37.563	33.3	5.5	2.2	3.6
19SG	2015–2020	UC San Gregorio net	15.115	37.564	44.1	9.5	1.9	3.1
21SG	2015–2017	UC San Gregorio net	15.116	37.564	35.4	6.5	2.8	5.0
22SG	2015–2017	UC San Gregorio net	15.118	37.564	43.3	4.2	2.8	4.7
28AT	2014–2016	UC Acitrezza net	15.160	37.561	32.9	12.8	7.6	12.5
32AT	2014–2018	UC Acitrezza net	15.155	37.563	48.3	14.5	3.1	5.1
33AT	2014–2018	UC Acitrezza net	15.156	37.561	48.7	10.5	3.1	6.0
37AT	2014–2016	UC Acitrezza net	15.153	37.561	34.5	11.7	5.7	12.2
38AT	2014–2016	UC Acitrezza net	15.155	37.560	21.0	15.9	6.5	10.6
39AT	2014–2016	UC Acitrezza net	15.147	37.564	70.7	−4.1	4.1	7.5
44AT	2014–2018	UC Acitrezza net	15.140	37.564	56.2	9.0	6.2	5.1
45AT	2014–2018	UC Acitrezza net	15.142	37.563	41.9	1.2	5.2	4.4
46AT	2014–2018	UC Acitrezza net	15.143	37.562	30.9	9.5	5.4	7.2
NFW1	2018–2020	UC Nizzeti net	15.118	37.585	75.9	4.6	10.4	18.2
NFW2	2018–2020	UC Nizzeti net	15.125	37.599	61.8	22.2	11.0	18.1
NFE3	2018–2020	UC Nizzeti net	15.146	37.592	80.7	0.6	11.1	18.8
NFE4	2018–2020	UC Nizzeti net	15.139	37.578	90.7	−6.1	10.9	20.2
BOL2	2018–2020	UC Belpasso-Ognina net	15.124	37.536	31.7	10.5	11.4	20.4
BOL3	2018–2020	UC Belpasso-Ognina net	15.098	37.546	28.0	9.0	912.9	21.6
BOL4	2018–2020	UC Belpasso-Ognina net	15.084	37.531	27.6	3.3	8.1	13.6
BOL5	2018–2020	UC Belpasso-Ognina net	15.072	37.551	35.0	7.0	10.7	20.0
BOL6	2018–2020	UC Belpasso-Ognina net	15.054	37.552	35.7	2.2	9.5	17.1

The slip rate on the northern block of the Tremestieri–San Gregorio–Acitrezza fault system increases from west to east. This is particularly clear for the periods 2016 and 2018 (see Supporting Information S3). We found a right lateral slip rate of $\sim$ 30 mm yr^{-1} in 2016 and $\sim$ 20 mm yr^{-1} in 2018 for the eastern component. In 2019, it shows a slip rate of $\sim$ 60 mm yr^{-1} in its eastern part, decreasing to zero toward the west (Fig. 7). Using transverse sections, Bonforte *et al.* (2011) show that the San Gregorio–Acitrezza fault exhibits an abrupt increase in eastward motion of $\sim$ 15 mm yr^{-1} between the southern and northern blocks from 1995 to 2000.

Furthermore, further east, Urlaub *et al.* (2018) detected a 40 mm offset that occurred between 2017 May 12 and 20 across the offshore extension of the San Gregorio–Acitrezza fault.

According to Poland *et al.* (2017), the processes driving this fault are gravitational slip of the eastern flank and plastic deformation of the clays that form the Etna's basement.

4.3 The Belpasso–Ognina lineament

The Belpasso–Ognina lineament interacts with the compressional structures on northwest of Catania (Catania Anticline; De Guidi *et al.* 2015). Froger *et al.* (2001) show that this lineament creeped at a steady rate of $\sim$ 4 mm yr^{-1} between 1996 August and 1998 January. In addition, Solaro *et al.* (2010) and Bonforte *et al.* (2011) observe an increase of the eastward velocity of $\sim$ 5 mm yr^{-1} from southwest to northeast along the entire lineament.

From 2016 to 2019, the maximum rate of relative motion across the Belpasso–Ognina lineament was $\sim$ 20 mm yr^{-1}, which occurred in 2018 in the northern block (see Supporting Information S3).

In 2016, it was active only in its eastern part of $\sim$ 7 mm yr^{-1} for the east component (see Supporting Information S3).

In 2018, the northern block of the lineament shows an eastward offset of $\sim$ 20 mm yr^{-1} and an offset of at least $\sim$ 3 mm yr^{-1} at the fold axis of the Catania anticline on the vertical component. For the upward component, it shows an offset of $\sim$10 mm yr^{-1} (see Supporting Information S3) at the intersection of this structure with the Catania anticline.

In 2019, the lineament shows no significant offset on the eastern component, but when considering the upward component, it shows an uplift of $\sim$ 8 mm yr^{-1} in the central part on both the northern and southern blocks without any offset (Fig. 7).

5 DISCUSSION

5.1 Eastward sliding

The GNSS stations close to the Ionian coast (ERIP, ELEO, EPOZ, ETEC and ELAC, Fig. 8) show a higher eastward velocity than

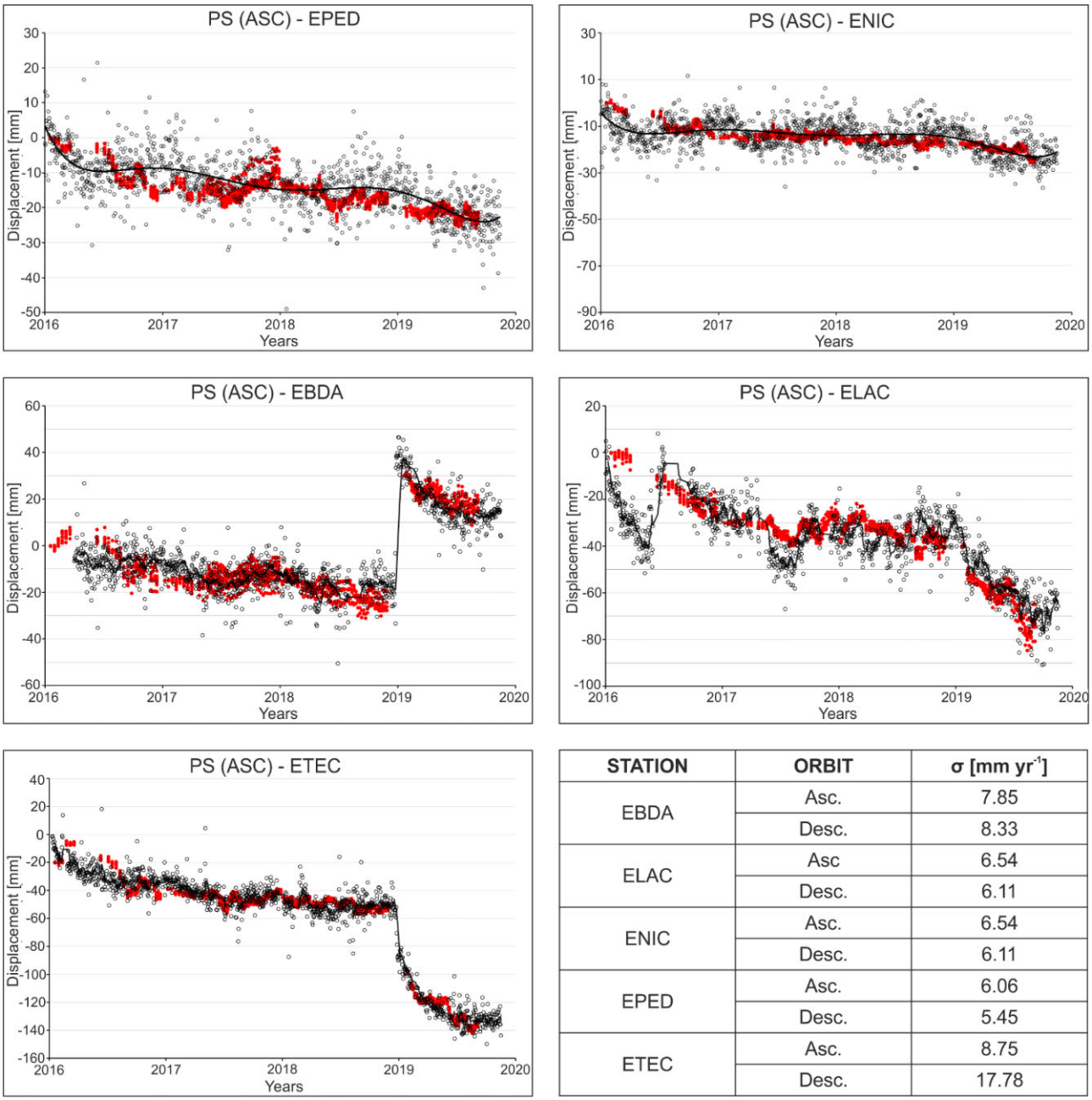

STATION	ORBIT	σ [mm yr^{-1}]
EBDA	Asc.	7.85
	Desc.	8.33
ELAC	Asc	6.54
	Desc.	6.11
ENIC	Asc.	6.54
	Desc.	6.11
EPED	Asc.	6.06
	Desc.	5.45
ETEC	Asc.	8.75
	Desc.	17.78

Figure 4. Alignment of PS (red dots) and GNSS LOS projected time-series (empty black dots) for the ascending track 44. The December 26 earthquake, following the onset of the eruption on December 24, produces the sharp displacements visible at the very end of 2018. On down right, the root mean square scatters of the alignment for each station and orbit are shown. The root mean square was calculated respect the residual between PS data and the LOS-projected GPS data.

those on the central flank of Etna (EMFN, ESPC, EC10, EPED and ENIC). This eastward slip affects the entire eastern flank (Bonforte & Puglisi 2006; Bonforte *et al.* 2008; Branca *et al.* 2014). This eastward motion is accommodated by the normal faults located on the central eastern flank of Etna: the Linera, Santa Venerina, San Leonardello, Fiandaca and Nizzeti faults.

The time-series of the GNSS stations (Fig. 8) located on the central flank of Etna (ENIC and EPED) are less affected by the eastward movement, and the episodic inflation and deflation cycles of the volcano are more visible at these stations, especially in the northern and upper components. ENIC and EPED, for example, show a southward trend change in their northern component from mid-2018 due to the inflation phase that preceded the onset of volcanic unrest of the 2018 eruption. During the period from 2001 to 2019, ENIC shows at least six variations in its northern component, corresponding to inflation and deflation phases of the volcano (Fig. 8). However, the quasi-constant azimuth velocity of some permanent stations on the lower eastern flank, for example, EBAG, ELEO, EPOZ and ELIN indicates that the eastern flank is affected by both extensional tectonic dynamics and eastward sliding. This suggests that either the decollement surface is deeper than the structures, or that the structures, although related to the regional extensional dynamic, are affected by the gravitational sliding of the Etna's eastern slope.

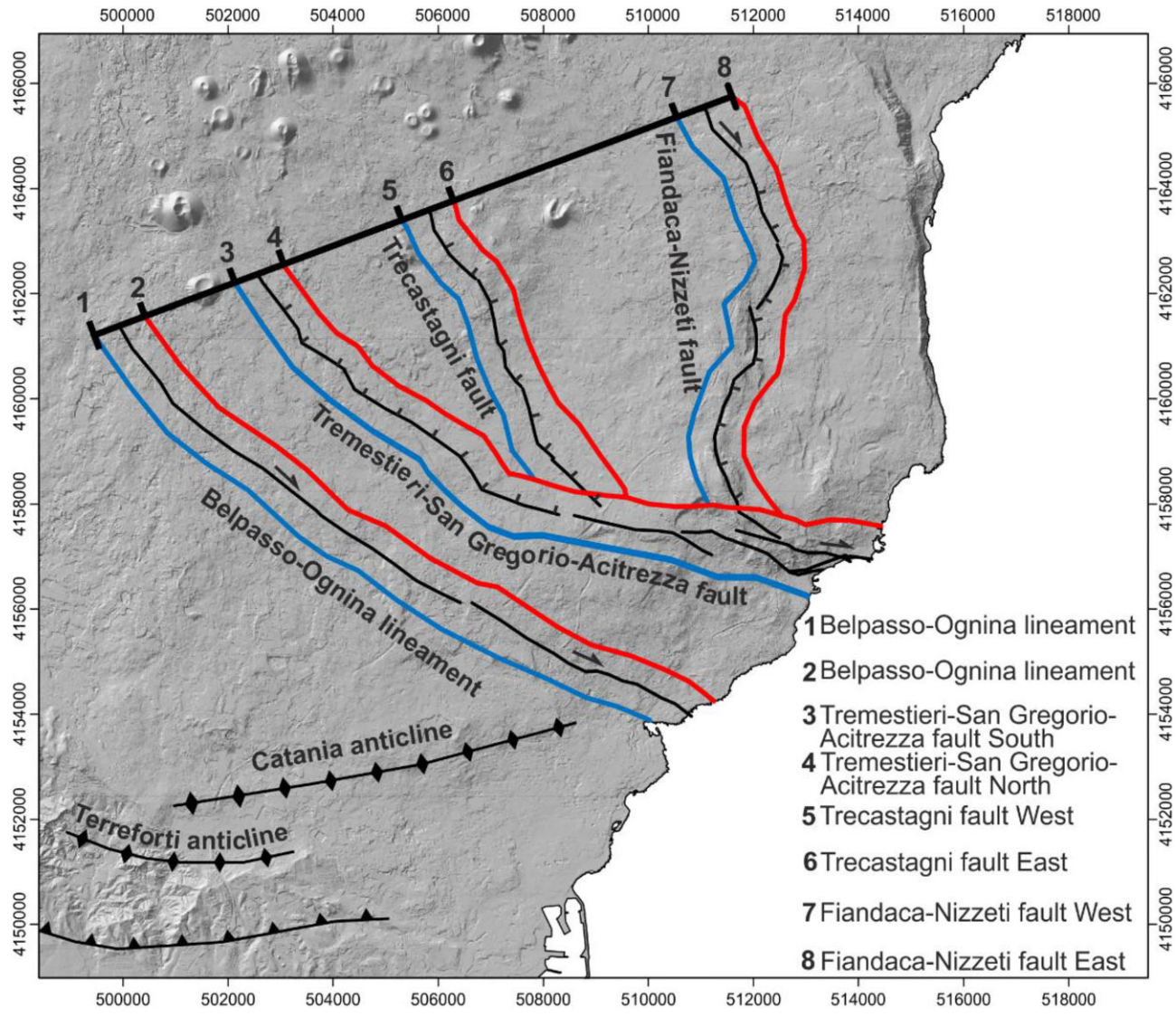

Figure 5. Trace of the profile used to select and to plot the permanent scatters along the fault in red (east and north profiles from the faults) and light blue (west and south profiles from the faults). The course black line represents the zero common to all profiles.

5.2 The 2018 December 26 earthquake

The 2016–2019 GNSS and PS, selected within a distance buffer of 50 m from a profile connecting the EBDA and ETEC GNSS stations, (Fig. 9) show the constant eastward velocity trend of the eastern flank until the end of 2018. From October to December 2018, the velocity inversion on the time-series is evident, suggesting the onset of the yield phase of the coseismic deformation.

The GNSS time-series (Fig. 8) show how the eastward velocity was strongly influenced by the intrusion of dykes beneath the centre of the volcano and the subsequent $M_w = 4.9$ earthquake of 2018 December 26.

Coseismic displacements have been recorded at all permanent GNSS stations on Etna's eastern flank. EBDA, located closest to the epicentre on the footwall of the fault, recorded the largest coseismic displacement of ∼60 mm on the north component, ∼−40 mm on the east component and ∼15 mm on the vertical component (Fig. 8). EPED and ENIC, located at about 6 and 9 km southwest from the epicentre, recorded displacements of ∼8 and ∼4 mm on the east component, respectively (Fig. 8). Looking at the northern component of these stations, ENIC recorded a northward motion during and after the earthquake, which could be related to a deflation phase of the Mount Etna; instead, EPED records no slip or strain on the northern component.

ETEC, located to the east of the Fiandaca fault at a distance of ∼ 5 km from the epicentre, records a displacement of ∼ 50 mm on the east component and ∼−40 mm on the north component (Fig. 8). There are two faults between ETEC and the epicentre, which probably accommodated part of the deformation.

5.3 Deformations following the 2018 crisis

To analyse the post-seismic deformation, we considered the 2019 time-series of ETEC and EBDA stations, together with the PSs time-series locali-zed along a profile between these two stations.

During the post-seismic period, the eastward acceleration is observed with the same magnitude by both EBDA station and the nearest PSs, despite their dispersion (orange dots in Fig. 10). At the same time, an eastward acceleration is observed at the GNSS ETEC

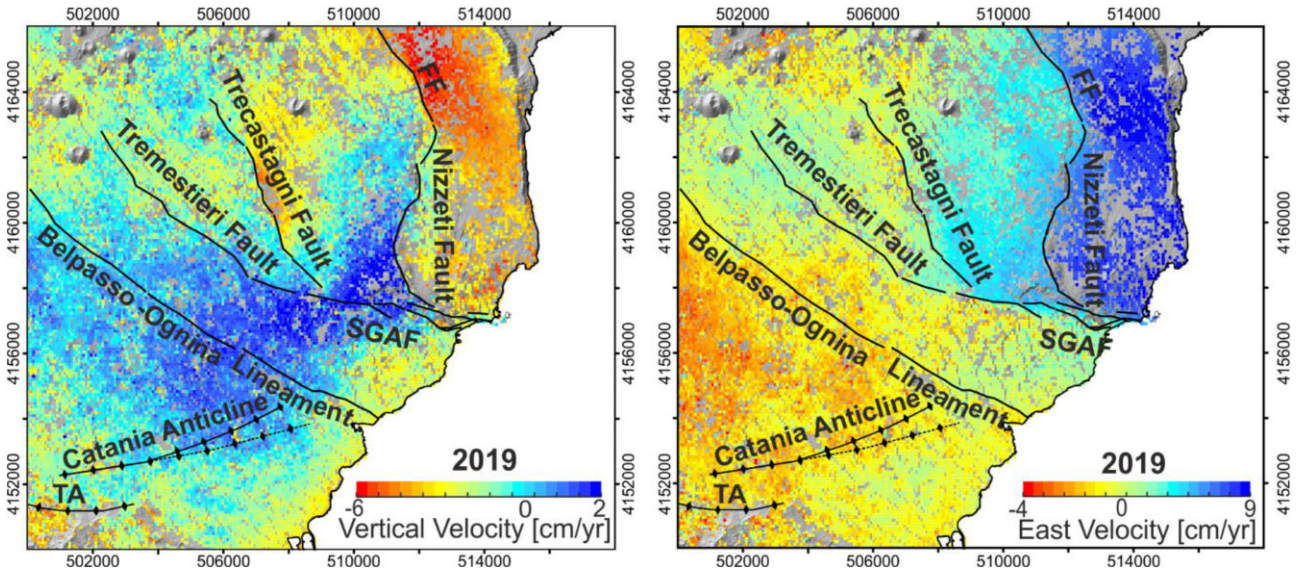

Figure 6. Vertical velocity map (on the left) and East velocity map (on the right) of PSs recorded during the 2019. TA Terreforti anticline; SGAF San Gregorio Acitrezza fault; and FF Fiandaca fault.

station, which is underestimated by the PSs in the vicinity of the GNSS station (green dots in Fig. 10).

We obtained a value of relaxation time value of $\sim 77 \pm 25$ d for the GNSS ETEC station. ETEC, located on the hangingwall of the Linera fault, records a higher acceleration than EBDA. This suggests that the Timpe fault system (Linera, Santa Venerina and Sant'Alfio Guardia faults) promotes the eastward acceleration of the unstable eastern flank of the volcano. The hangingwall of the Linera fault has an eastward velocity greater than of the footwall, indicating that this eastward acceleration is controlled by a gravitational slip and is driven by the tectonic origin of this fault system.

The PSs located near ETEC (green dots in Fig. 10) show a displacement greater than that recorded by the PSs between the two faults (red dots in Fig. 10). They also show two jumps, probably due to an unwrapping bias, on 2019 June 14 and August 07, suggesting that the total displacement may be underestimated. The intermediate PSs show a displacement larger than EBDA and smaller than ETEC (red dots Fig. 10), and the velocity of the PSs increases from west to east. This further suggests that the gravitational behaviour of the system, interspersed with elastic failures, increases towards the sea and perhaps further offshore.

In addition, the PDAP and MDGR campaign points (Fig. 3) also show an increase in the velocity in the eastern component relative to their long-term velocity (Supporting Information, S1).

5.4 The kinematic of Acitrezza fault

In Carnemolla (2021), a local reference system allows the analysis of the fault offset: by grouping the stations located on the north of the San Gregorio–Acitrezza fault, an eastward right lateral movement of $\sim 15 \pm 2$ mm yr^{-1} is recorded (Fig. 3a). Moreover, grouping the points of the Acitrezza network to the north of the SGAF and referring to the same local reference system, a right lateral motion of 23.5 ± 3 mm yr^{-1} between the blocks is found for the period 2015–2020, while grouping the stations to the south there is a residual with respect to the 02SG of 3 ± 6 mm yr^{-1}. The time-series suggest that, considering the stations in the northern block of the SGAF, the eastward velocity increases by ~ 8 mm yr^{-1} between the San Gregorio network and the Acitrezza network. This result supports the model proposed by De Guidi *et al.* (2018), in which the Nizzeti fault accommodates this extension of ~ 8 mm yr^{-1}.

The ELAC GNSS station shows the most variable velocity in the time-series of the whole GNSS network (Fig. 11). It is characterized by a variable velocity previously mentioned by Mattia *et al.* (2015, 2020), Palano (2016), Bruno *et al.* (2017), De Guidi *et al.* (2018) and Palano *et al.* (2022). Between 2016 and 2019, this station shows at least 5 SSEs, 3 of them occurred after the volcano-tectonic crisis of 2018 December.

To analyse the deformation that occurred along the Acitrezza fault, we selected the PSs located at 500 m north and south of the fault (see Supporting Information S5). We analysed the time-series of these PSs together with the time-series of the GNSS station ELAC.

Since October 2018, ELAC shows a decrease of the eastward velocity that ended shortly after the volcano-tectonic crisis of 2018 December 24–26 (Fig. 12).

For the year 2019, by a visual inspection of the ELAC time-series for 2019, we found three jumps (Fig. 13):

(i) From 2019 January 14 until February 5; this jump is not assimilable to a typical SSE because lasts at least 22 d and, so we prefer to define it as a long slip event (LSE). The first part shows a typical SSE with a displacement of $\sim$10 mm over 20 d, and a second part with a duration of two days with a displacement of $\sim$ 15 mm. This LSE could be considered as the beginning of yielding phase before and after the rupture.

(ii) On 2019 April 2; attributed to an SSE with a displacement of $\sim$ 8 mm with a duration of one day.

(iii) On 2019 June 20; attributed to an SSE with a displacement of $\sim$ 10 mm with a duration of one day.

The northern PSs show a trend similar to that of ELAC but with a smaller displacement, while the southern PSs do not show the same jumps as ELAC.

In the north, we analysed in detail the time-series of three PSs located north of the fault: N7, N9 and N6 (Fig. 13):

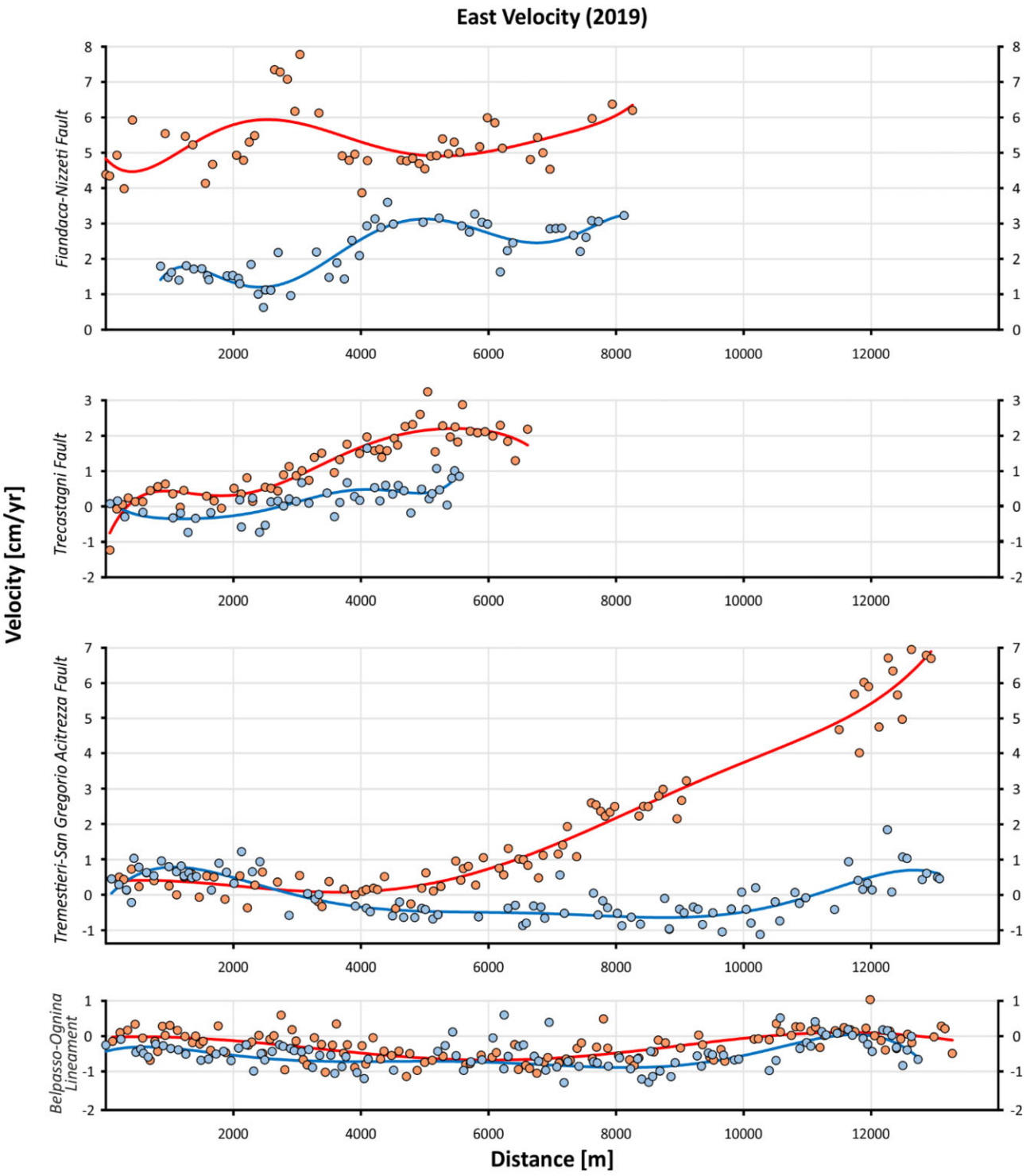

Figure 7. East velocity profiles of the selected PS for the Fiandaca–Nizzeti, Trecastagni, Tremestieri–San Gregorio Acitrezza faults and for the Belpasso–Ognina lineament, for the 2019. Blue dots are the south or west profiles. The red dots are the north and east profiles.

(i) From 20 January 2019 to 3 April 2019, the N7, in the west, is the fastest.

(ii) From 3 April 2019 until 26 June 2019, the N9, in the centre, is the fastest.

(iii) From 26 June 2019, the PS N7 is the slowest, while points N6 and N9 have approximately the same velocity.

Probably these PSs show that the deformation varies from west to east along the fault during the 2019, as observed along the strike-slip faults, but this hypothesis need future investigation carried out by new GNSS stations along the Acitrezza fault. After the SSE3, there is an inconsistency between ELAC and the PSs to the north; the PSs show a higher velocity than the ELAC. We suggest three reasons for this inconsistency:

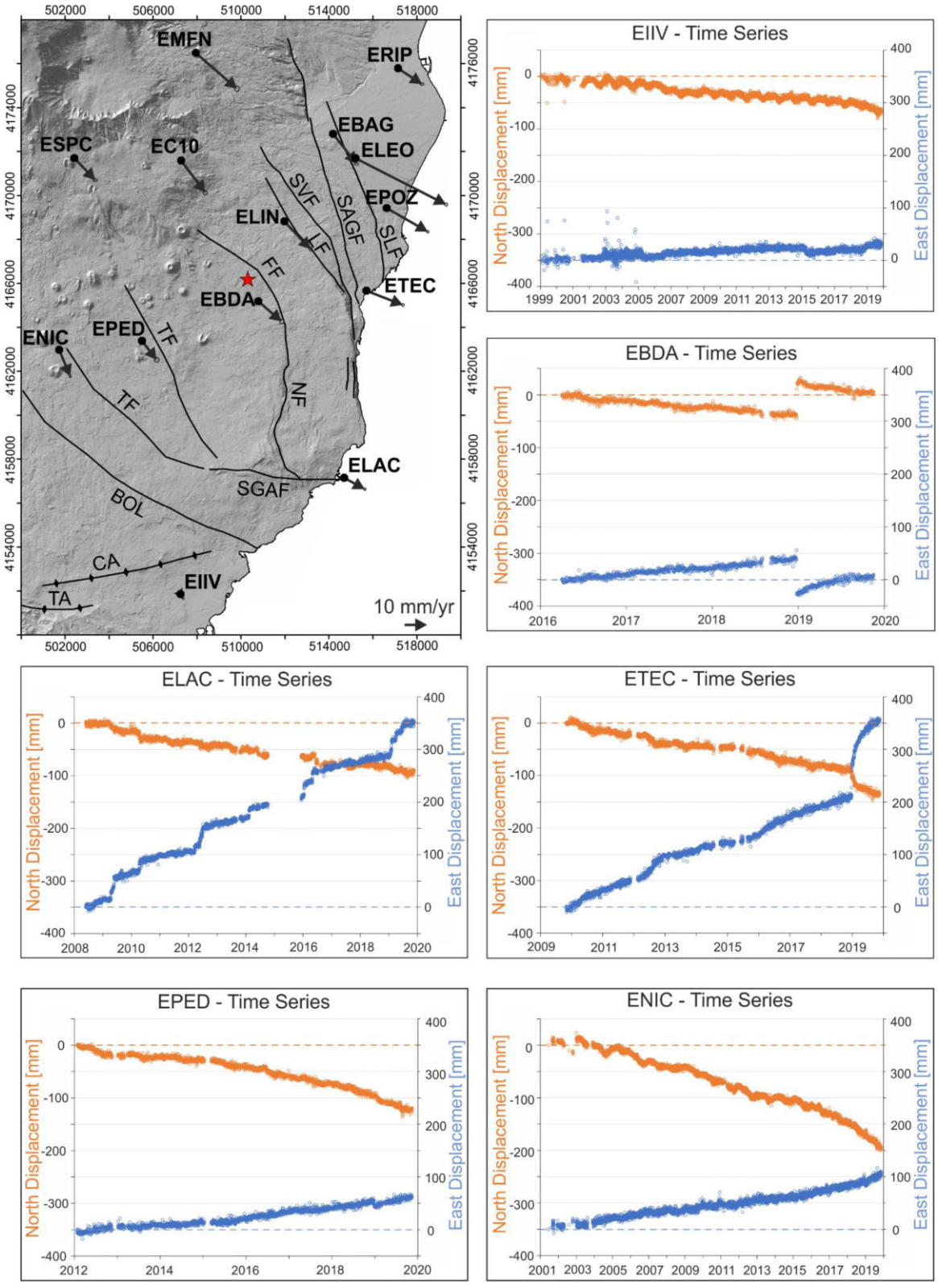

Figure 8. On the top left, the velocity field of the eastern flank of Mount Etna is show; SVF Santa Venerina, SAGF Sant'Alfio-Guardia, SLF San Leonardello, LF Linera faults and TA Terreforti Anticline. Red star represents the epicentre of the $M_w = 4.9$ earthquake of 2018 December 26. The time-series of the GNSS permanent stations: EIIV, EBDA, ELAC, ETEC, EPED and ENIC are show. The velocity field and time-series are referred to eastern Sicily.

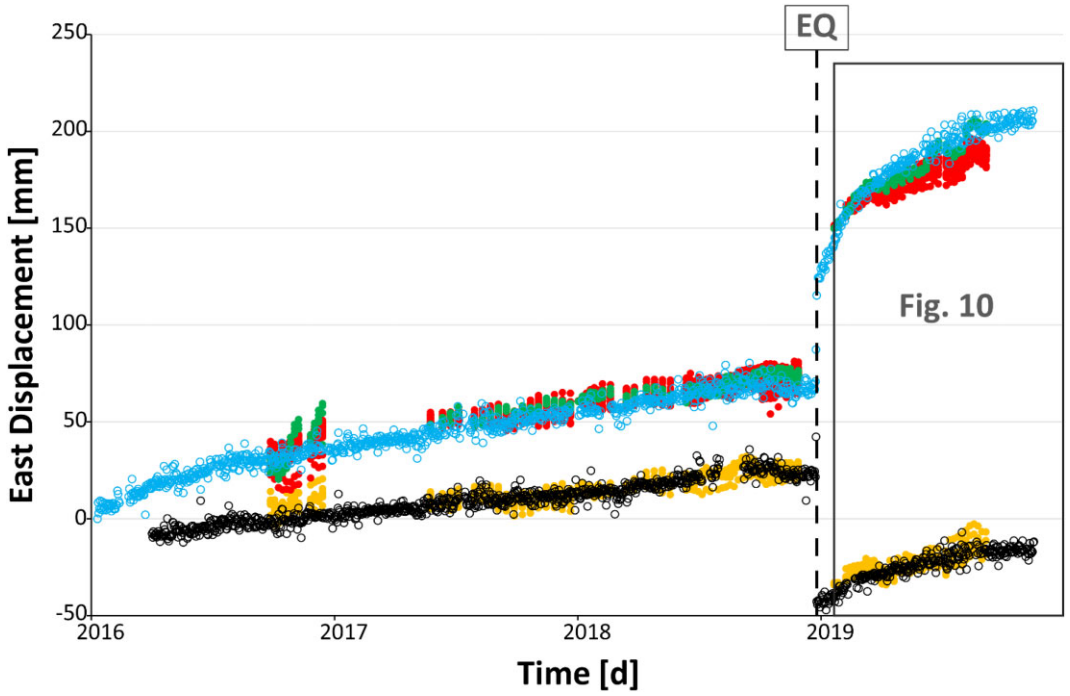

Figure 9. Time-series of the GNSS stations EBDA (black empty dots) and ETEC (light blue dots) and the PS selected along the profile. Orange points are the PS located between the GNSS station EBDA and the Fiandaca fault; red points are the PS located between the Fiandaca and the Linera faults and green points are the the PS located between Linera Fault and the GNSS station ETEC. See Supporting Information S5 for location of the PSs.

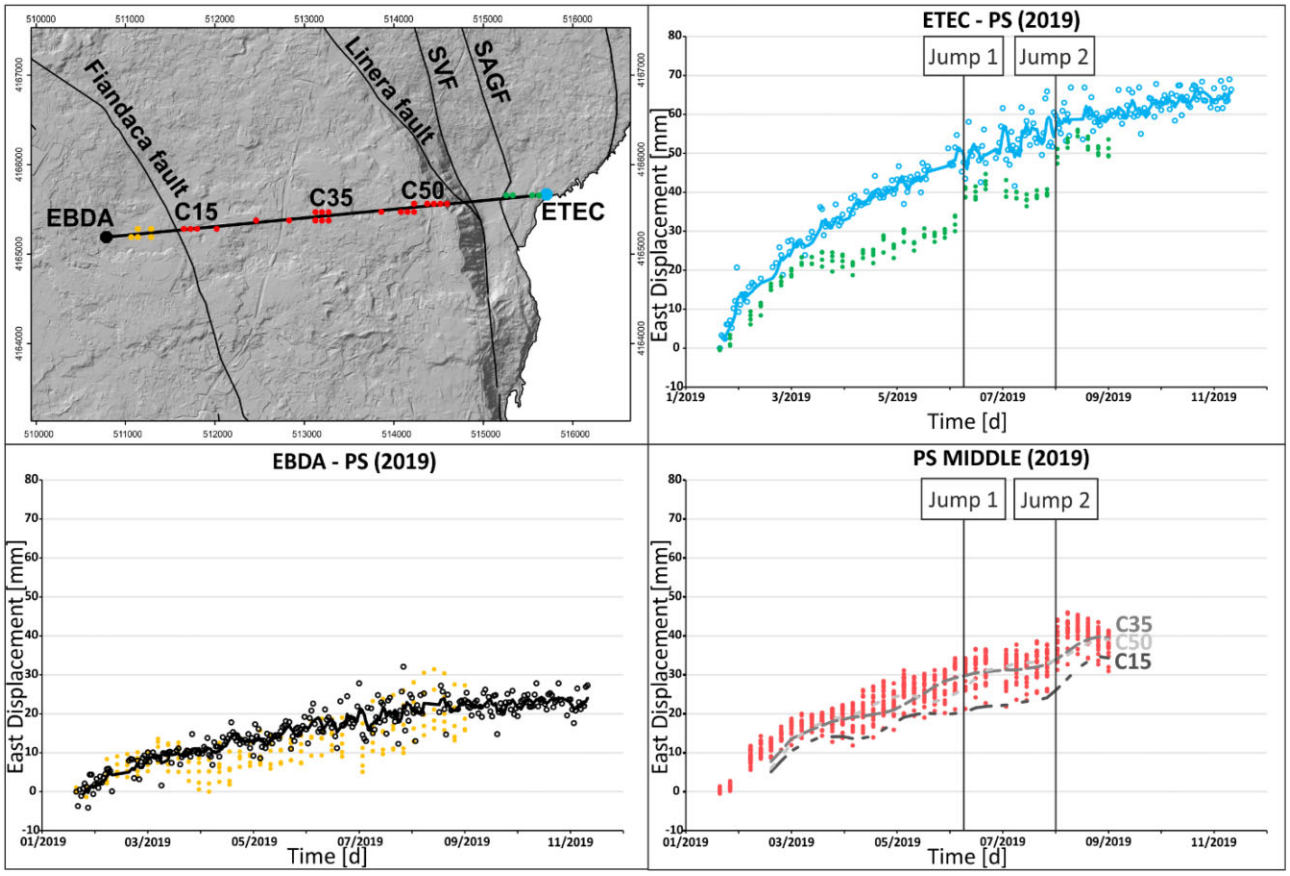

Figure 10. The 2019 time-series of the GNSS stations EBDA (black empty dots) and ETEC (light blue dots) and the PS selected along the profile. Orange points are the PS located between the GNSS station EBDA and the Fiandaca fault; and red points are the PS located bet between Linera Fault and the GNSS station ETEC. The grey dashed line is the moving average of the C35, the grey dotted–dotted lines is the moving average of the C50 and the grey dashed–dotted–dotted point is the C15.

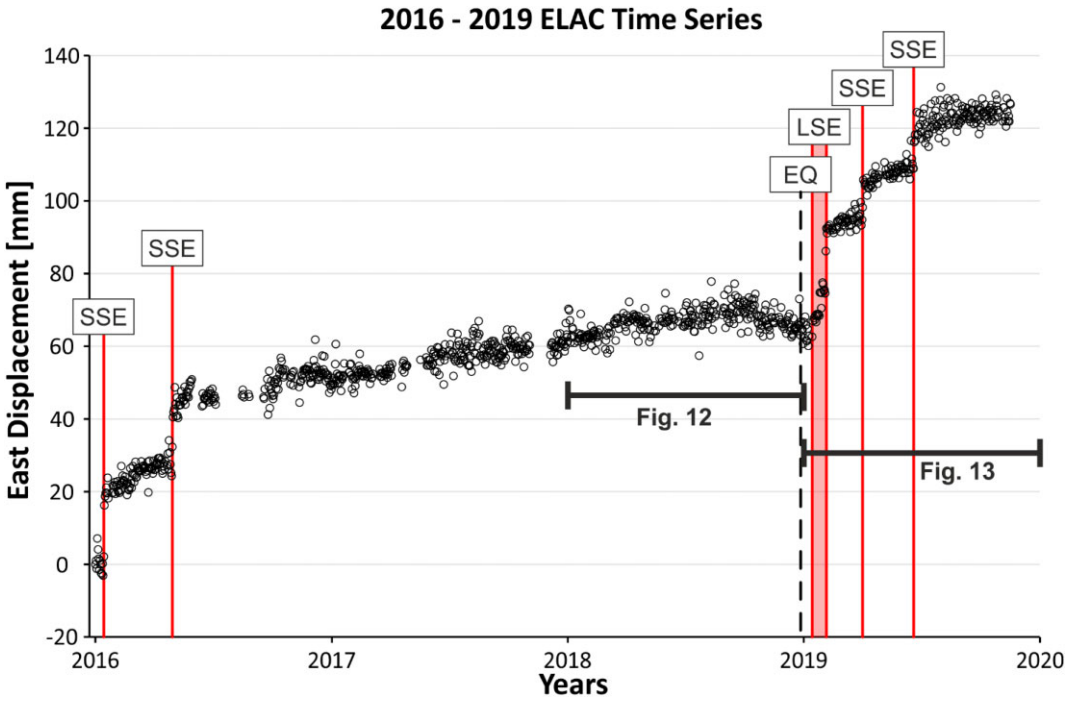

Figure 11. 2016–2019 east displacement time-series of the GNSS station ELAC. Red line are the SSEs detected during this period; and black dashed line is the earthquake of 2018 December 26.

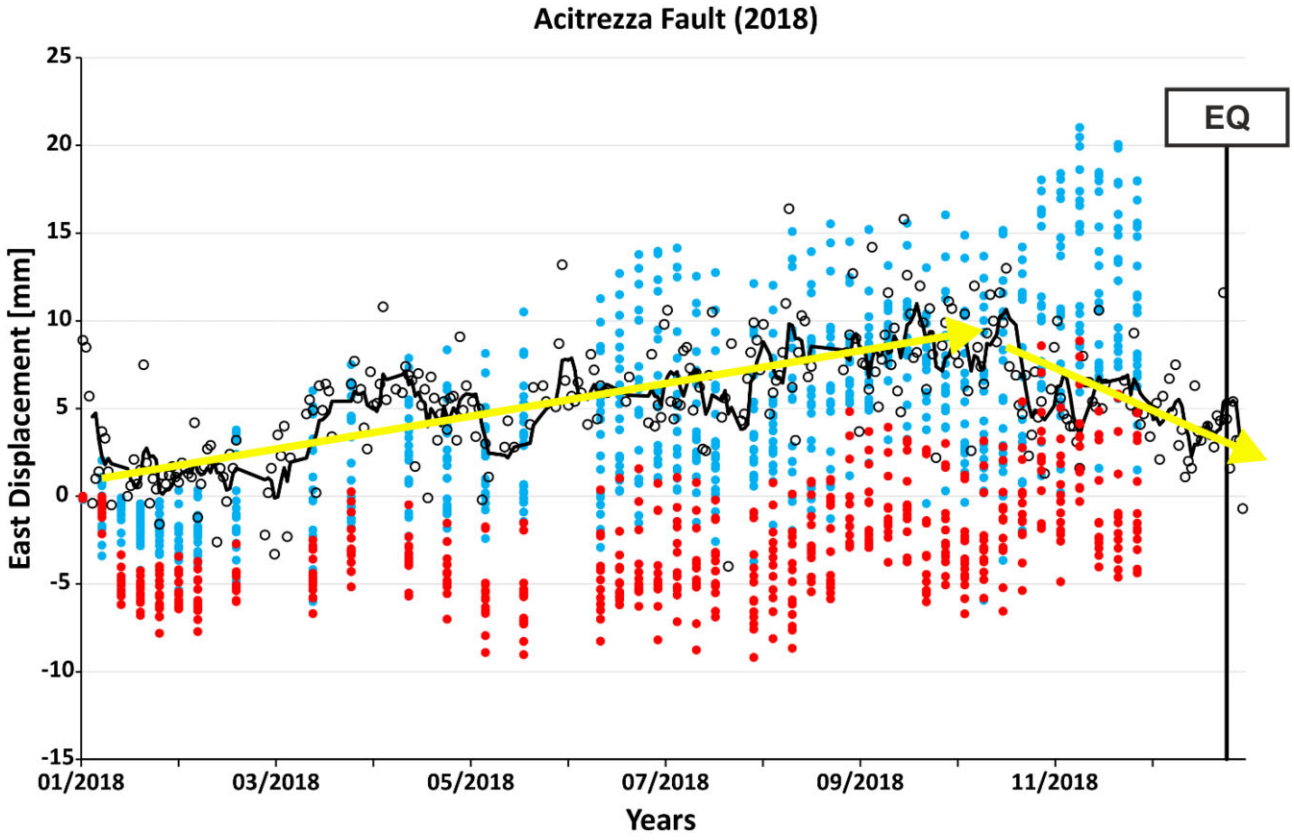

Figure 12. Time-series (01/01/2018–31/12/2018) of the PS located on the North (blue) and on the South (red) of the Acitrezza fault. The east component time-series of ELAC is shown (empty black dots). The black line represents the earthquake occurred on 2018 December 6 on Mount Etna. Yellow lines represent the linear trend detected from 2018 January 2018 until October and from 2018 October to December. See Supporting Information S5 for the location of the PSs.

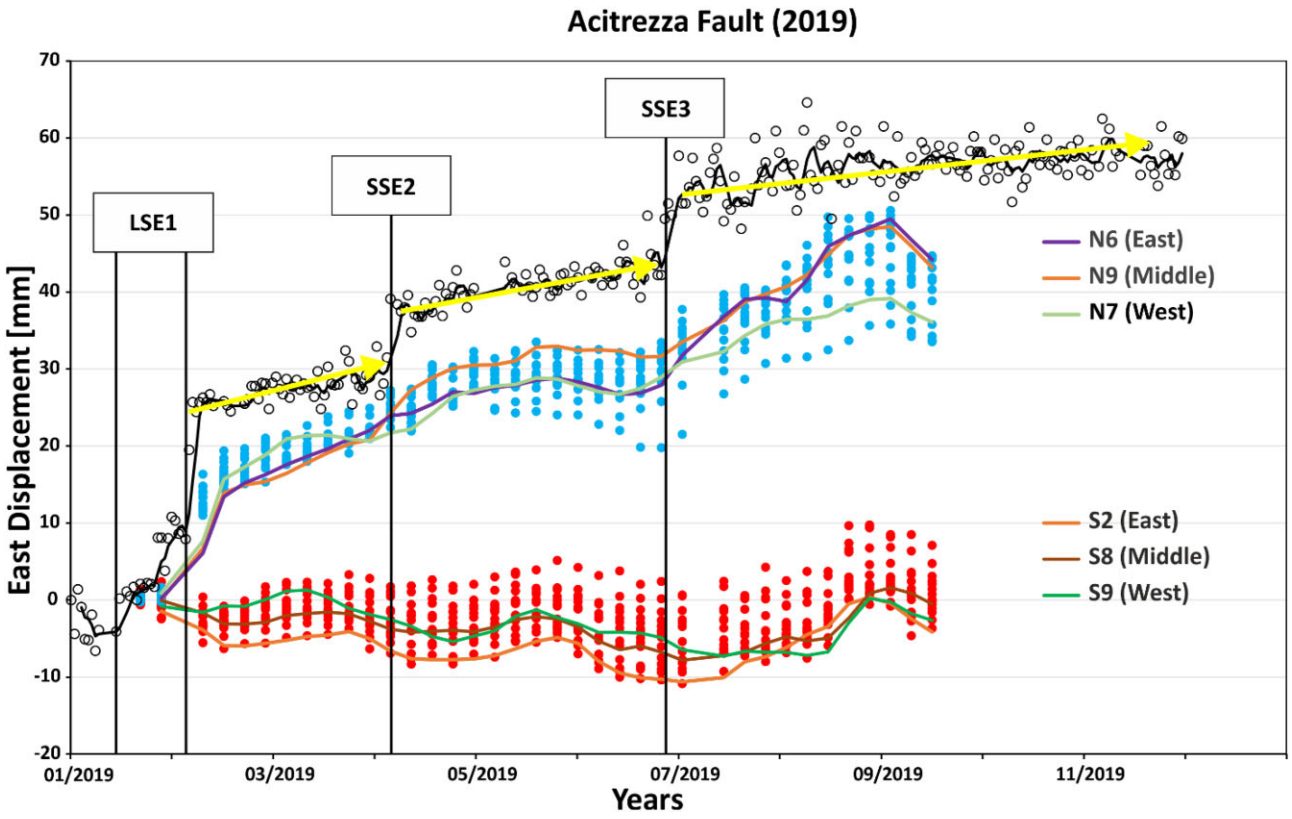

Figure 13. Time-series (01/01/2019–17/11/2019) of the PS located on the North (blue) and on the South (red) of the Acitrezza Fault. The time-series of ELAC is shown (empty black dots). See supplementary Material S5 for the location of the PSs.

(i) Uncorrected phase unwrapping within the P-SBAS tool.

(ii) SSE3 'propagates' to the west and is therefore recorded later by the PSs than ELAC if we considered the source of creep located below ELAC.

(iii) The large noise in the ELAC time-series (> 10 mm) after SSE3 is also recorded by the PS.

5.5 The role of Belpasso–Ognina lineament

The GNSS and PS data for the Belpasso–Ognina lineament suggest that it has a right-lateral kinematics. This lineament is affected by deformation due to the NNW-SSE regional compressional dynamics and subsequently by volcanic activity. Analyses of the velocity profiles (Fig. 7 and Supporting Information S3) along this structure shows that the right-lateral kinematics is constant over the four years with a general eastward trend of the area. This lineament intersects the Catania anticline at its eastern end. The Catania anticline determines a vertical velocity differential between the two blocks of the lineament along the anticline axis. On average, the southern block has a greater uplift than the northern block.

In 2016, it shows a right lateral movement and a general uplift with a different velocity between the northern and southern blocks. This suggests that the Catania anticline is active on the southern block of the Belpasso–Ognina lineament and less active on the northern block.

In 2017, the Belpasso–Ognina lineament does not show any significant offset in eastern and vertical components.

In 2018, the Belpasso–Ognina lineament is affected by deformation due to the activity of the Catania anticline. Looking at the eastern component, we identified an offset of ∼3 mm yr^{-1} (see Supporting Information S3). It is located west of the intersection with the Catania anticline. The vertical velocity shows the activity of the anticline to the south-west of the lineament (see Supporting Information S4).

In 2019, however, this lineament is affected by a homogeneous deformation following the volcanic unrest of 2018 December and does not show any significant offset.

GNSS data from the Belpasso–Ognina UNICT subnetwork confirm the right-lateral kinematics of this fault (Fig. 3a). The GNSS point BOL4 records the deformation due to the activity of the Catania anticline because it has a different azimuth velocity compared to the other points of the same subnetwork. Moreover, BOL4 shows a significant deformation compared to that recorded by the EIIV station, so the differential fold deformation is accommodated by the Catania anticline.

6 CONCLUSION

Considering the velocity of GNSS stations (e.g. EBAG, ELEO, EPOZ and ELIN) on the mid-eastern flank (Figs 2 and 8), we inferred that the Timpe fault system contributes to the gravitational slip of the eastern flank, superimposed on the regional extensional dynamic.

Our results confirm, for a different time period, those obtained by De Guidi *et al.* (2018). We suggest that the Nizzeti fault is affected by an east–west extension of ∼ 8 mm yr^{-1} due to the activity of the San Gregorio–Acitrezza fault. According to the models (e.g. those of Brober 1999; Walsh *et al.* 2002) and observations (e.g. those of De Guidi *et al.* 2017), the fault terminations represent the areas of maximum concentration of elastic stress, so we propose to install

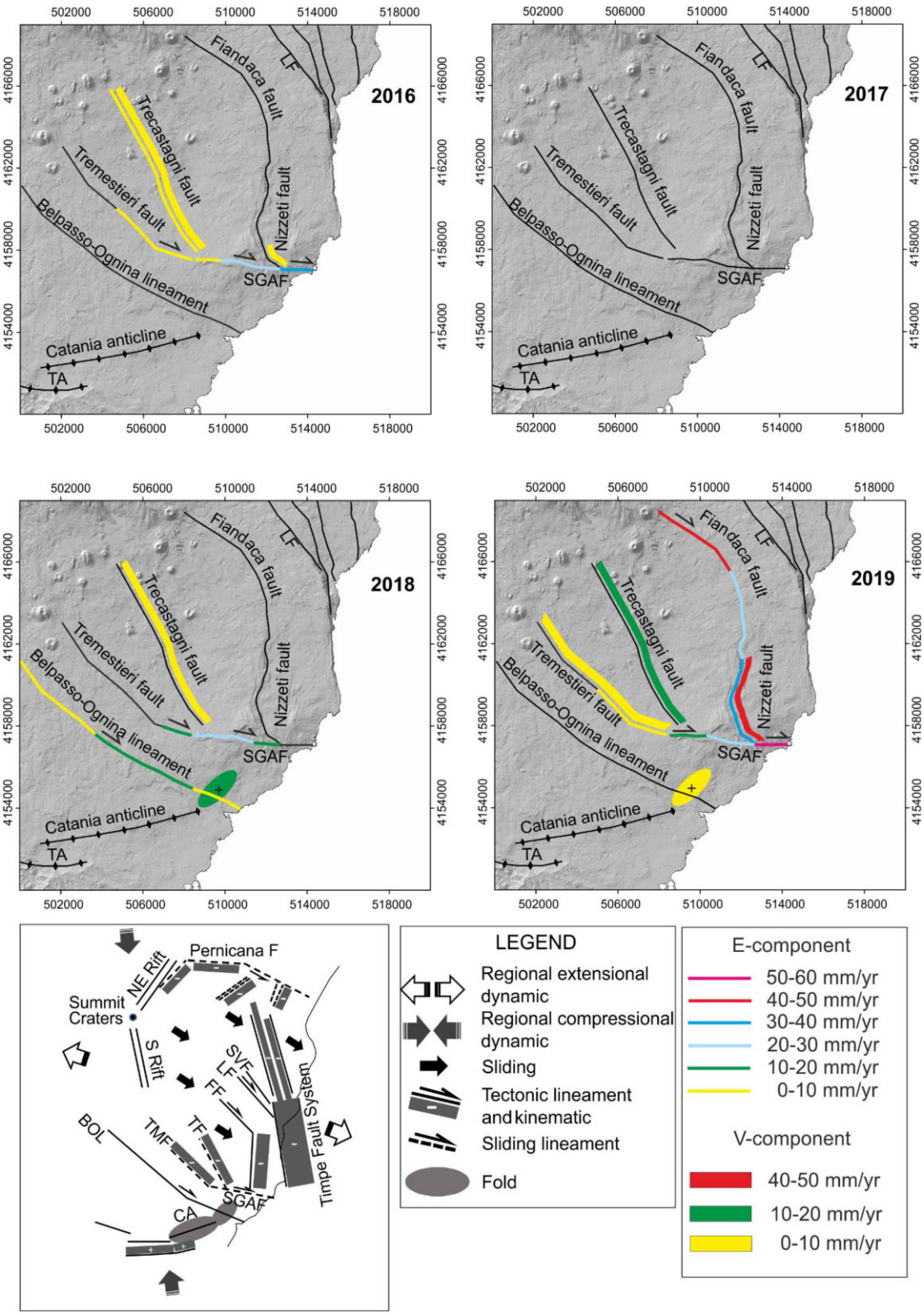

Figure 14. On the top and middle, schematic morphtectonic map of the eastern flank of Etna showing the concentration of deformation occurred on 2016, 2017, 2018 and 2019. On the bottom left, schematic volcano-tectonic model showing the regional and local dynamics together with the tectonic and sliding lineament. TA Terreforti anticline; LF Linera fault; SGAF San Gregorio Acitrezza fault; SVF Santa Venerina fault; FF Fiandaca fault; TF Trecastagni fault; TMF Tremestieri Fault; BOL Belpasso Ognina lineament and CA Catania Anticline.

a permanent GNSS network along this fault to further investigate transient deformation.

The San Gregorio–Acitrezza fault has been associated with the SSEs recorded by the ELAC permanent GNSS station, but this area requires further study to define a model of these aseismic events, together with the surface involved and the relationship with the clays outcropping in this area. In particular, it would be essential to acquire further deformation data parallel and transversely to this fault, together with microseismicity in order to discriminate the depth and extent of the aseismic creep source.

The same need exists for the area of village of San Gregorio, where the Tremestieri and Trecastagni faults join the San Gregorio–Acitrezza fault. The GNSS data of the Belpasso-Ognina network and the EIIV station indicate that the San Gregorio–Acitrezza fault accommodates most of the deformations of the unstable eastern flank.

The Belpasso–Ognina lineament plays a fundamental role in the distribution and concentration of the regional and local stress field, and was also stressed during the volcanic unrest at the end of 2018. We show that the flank dynamics disappear completely south of this lineament and the regional stress dominates the volcanism.

Furthermore, considering the EIIV GNSS station and the points of Belpasso–Ognina subnetwork, we found a differential velocity suggesting that the deformation of the Catania anticline disappears the south, but EIIV stations still records the activity of the incipient decollement folding (Figs 2b and 3a, De Guidi *et al.* 2015). Finally we suggest that the Belpasso–Ognina lineament accommodates the regional compressive dynamic deformation as a tear fault (Huang *et al.* 2006; Nishimura *et al.* 2008; Belabbès *et al.* 2009) but this conclusion needs to be confirmed by further investigation.

We construct a tectonic model that illustrates the motion of the blocks between the various faults on which we observe the concentration of deformation by relative motion of the different parts of the flank that yearly summarizes the results (Fig. 14).

The 2016–2019 PS time-series are not systematically consistent with the GNSS data. As a result, we decided to perform additional processing for each year from 2016 to 2019 to align the PS data with the GNSS data. It was found that the alignment was good for the stations with a constant deformation rate, while for the stations with a non-constant deformation rate, the P-SBAS data were not always consistent with the GNSS data. This result shows that the P-SBAS processing algorithm (Casu *et al.* 2014; de Luca *et al.* 2015; Manunta *et al.* 2019) is not always able to recover the true deformation, especially when it is highly nonlinear. This is particularly clear for the stations near the Ionian coast, especially ELAC and ETEC, which show abrupt velocity changes in their time-series, and for EBDA, which shows the coseismic deformation following the 2018 December earthquake.

ACKNOWLEDGMENTS

We are grateful to the Bachelor's and Master's degree students who helped us with the GNSS survey. Thanks are to the INGV-OE staff maintaining the GNSS permanent network. We thank Prof. Carmelo Monaco for the useful discussion about the volcano-tectonic aspect. We are grateful to the editor, assistant editor and two reviewers who helped us to improve the quality of the manuscript. This research has been supported by the PIAno di inCEntivi per la RIcerca di Ateneo (PIACERI 2020/2022) (Fund manager Giorgio De Guidi), the INGV project PIANETA DINAMICO, Theme ATTEMP (integrATed sysTEm for Mutli-hazard from sPace over mediTerranean) and the INGV project IMPACT (a multidisciplinary Insight on the kinematics and dynamics of Magmatic Processes at Mt. Etna Aimed at identifying preCursor phenomena and developing early warning sysTems).

DATA AVAILABILITY

Data are available on request by email to the corresponding author ('francesco.carnemolla@unict.it').

AUTHOR CONTRIBUTION STATEMENT

FC and PB processed and analysed the GNSS data. FC processed the Interferometric data by the P-SABS tool. AB provided the GNSS data of the campaign point of the INGV-OE network. FC, GDG and FB conducted the GNSS surveys of the points of the UNICT-Net. FC, GDG and PB wrote the paper. All the authors were involved in the conceptualization, discussion of the results and editing of the manuscript.

REFERENCES

Alparone, S., Barberi, G., Bonforte, A., Maiolino, V. & Ursino, A., 2011 Evidence of multiple strain fields beneath the eastern flank of Mt. Etna volcano (Sicily, Italy) deduced from seismic and geodetic data during 2003-2004, *Bull. Volcanol.,* **73**(7), 869–885.

Alparone, S. C. *et al.* 2022. Mt. Etna Seismic Catalog 2017-2019 (EtnaSC_2017_2019) (Version 1) [Data set]. INGV Publication: Rome, Italy..

Altamimi, Z., Rebischung, P., Métivier, L. & Collilieux, X., 2016. ITRF2014: a new release of the International Terrestrial Reference Frame modeling nonlinear station motions. *J. geophys. Res. Solid Earth,* **121,** 6109–6131.

Antonioli, F., Kershaw, S., Rust, D. & Verrubbi, V., 2003. Holocene sea-level change in Sicily and its implications for tectonic models: new data from the Taormina area, northeast Sicily. *Mar. Geol.,* **196,** 53–71.

Azzaro, R., Branca, S., Gwinner, K. & Coltelli, M.: 2012 The volcano-tectonic map of Etna volcano, 1:100.000 scale: an integrated approach based on a morphotectonic analysis from high-resolution DEM constrained by geologic, active faulting and seismotectonic data, *Ital. J. Geosci.,* **131**(1), 153–170.

Belabbès, S., Meghraoui, M., Çakir, Z. & Bouhadad, Y.: 2009 InSAR analysis of a blind thrust rupture and related active folding: the 1999 Ain Temouchent earthquake (M w 5.7, Algeria) case study, *J. Seismol.,* **13**(4), 421–432, .

Berardino, P., Fornaro, G., Lanari, R. & Sansosti, E.(2002). A new algorithm for surface deformation monitoring based on small baseline differential SAR interferograms. *IEEE Trans. Geosci. Remote Sens.,* **40**(11), 2375–2383.,.

Bertiger, W. *et al.* 2020. GipsyX/RTGx, a new tool set for space geodetic operations and research. *Adv. Space Res.,* **66,** 469–489.

Boehm, J., Niell, A., Tregoning, P. & Schuh, H., 2006. Global Mapping Function (GMF): a new empirical mapping function based on numerical weather model data. *Geophys. Res. Lett.,* **33,** L07304. doi:10.1029/2005GL025546.

Bonaccorso, A., Bonforte, A., Guglielmino, F., Palano, M. & Puglisi, G.: 2006 Composite ground deformation pattern forerunning the 2004-2005 Mount Etna eruption, *J. geophys. Res. Solid Earth,* **111**(B12), https://doi.org/10.1029/2005JB004206.

Bonforte, A. & Puglisi, G.: 2006 Dynamics of the eastern flank of Mt. Etna volcano (Italy) investigated by a dense GPS network, *J. Volc. Geotherm. Res.,* **153**(3–4), 357–369 .

Bonforte, A., Bonaccorso, A., Guglielmino, F., Palano, M. & Puglisi, G.: 2008 Feeding system and magma storage beneath Mt. Etna as revealed by recent inflation/deflation cycles, *J. geophys. Res.,* **113**(B5), B05406, doi:10.1029/2007JB005334 .

Bonforte, A., Federico, C., Giammanco, S., Guglielmino, F., Liuzzo, M. & Neri, M.: 2013 Soil gases and SAR measurements reveal hidden faults on the sliding flank of Mt. Etna (Italy), *J. Volc. Geotherm. Res.,* **251,** 27–40.

Bonforte, A., Guglielmino, F., Coltelli, M., Ferretti, A. & Puglisi, G., 2011. Structural assessment of Mount Etna volcano from Permanent Scatterers analysis. *Geochem. Geophys. Geosyst.,* **12,** https://doi.org/10.1029/2010GC003213.

Bonforte, A. *et al.* 2016. Global positioning system survey data for active seismic and volcanic areas of eastern Sicily, 1994 to 2013. *Sci. Data,* **3,** 160062. https://doi.org/10.1038/sdata.2016.62.

Bonforte, A., Guglielmino, F. & Puglisi, G., 2019 Large dyke intrusion and small eruption: the December 24, 2018 Mt. Etna eruption imaged by Sentinel-1 data, *Terra Nova,* **31,** 405–412.

Borgia, A. *et al.* 2000. Actively growing anticlines beneath catania from the distal motion of Mount Etna's Decollement measured by SAR interferometry and GPS. *Geophys. Res. Lett.,* **27,** 3409–3412.

Bousquet, J.-C. & Lanzafame, G., 1986. Déformations compressives quaternaires au bord sud de l'Etna. Comptes rendus l'Académie des Sci. Série 2, Mécanique, *Phys. Chim. Sci. l'univers, Sci. la Terre* 235–240.

Branca, S., De Guidi, G., Lanzafame, G. & Monaco, C., 2014 Holocene vertical deformation along the coastal sector of Mt. Etna volcano (eastern Sicily, Italy): implications on the time–space constrains of the volcano lateral sliding, *J. Geodyn.,* **82,** 194–203 .

Brober, K.B., 1999. *Cracks and Fracture*. Elsevier.

Bruno, V., Mattia, M., Montgomery-Brown, E., Rossi, M. & Scandura, D., 2017. Inflation leading to a slow slip event and volcanic unrest at Mount Etna in 2016: insights from CGPS data. *Geophys. Res. Lett.,* **44,** 12,141-12,149.

Carnemolla, F., 2021. What could be done to better monitor and understand the evolution of Etna faults? Monitoring and analysis of surface deformation using comparitive geodetic and topographyc techiniques. *Case Study of the Eastern Slope of the Etna Volcano*. PhD thesis, University of Catania.

Casu, F., Elefante, S., Imperatore, P., Zinno, I., Manunta, M., De Luca, C. & Lanari, R., 2014. SBAS-DInSAR parallel processing for deformation time-series computation. *IEEE J. Sel. Top. Appl. Earth Obs. Remote Sens.,* **7,** 3285–3296.

Catalano, S., Torrisi, S., Tortorici, G. & Romagnoli, G., 2011. Active folding along a rift-flank: the Catania region case history (SE Sicily). *J. Geodyn.,* **51,** 53–63.

D'Agostino, N., Avallone, A., Cheloni, D., D'Anastasio, E., Mantenuto, S. & Selvaggi, G., 2008. Active tectonics of the Adriatic region from GPS and earthquake slip vectors. *J. geophys. Res. Solid Earth,* **113,** 1–19.

D'Agostino, N. & Selvaggi, G., 2004. Crustal motion along the Eurasia-Nubia plate boundary in the Calabrian Arc and Sicily and active extension in the Messina Straits from GPS measurements. *J. geophys. Res. Solid Earth,* **109,** 1–16.

De Guidi, G. *et al.* 2015. Geological, seismological and geodetic evidence of active thrusting and folding south of Mt. Etna (eastern Sicily): revaluation of "seismic efficiency" of the Sicilian Basal Thrust. *J. Geodyn.,* **90,** 32–41.

De Guidi, G. *et al.* 2018. The unstable eastern flank of Mt. Etna volcano (Italy): first results of a GNSS-based network at its southeastern edge. *J. Volc. Geotherm. Res.,* **357,** 418–424.

De Guidi, G., Catalano, S., Monaco, C. & Tortorici, L., 2003. Morphological evidence of Holocene coseismic deformation in the Taormina region (NE Sicily). *J. Geodyn.,* **36,** 193–211.

De Guidi, G. *et al.* 2017. Brief communication: co-seismic displacement on 26 and 30 October 2016 (M w = 5.9 and 6.5)–earthquakes in central Italy from the analysis of a local GNSS network. *Natural Hazards Earth Syst. Sci.,* **17**(11), 1885–1892.

de Luca, C. *et al.* 2015. An on-demand web tool for the unsupervised retrieval of earth's surface deformation from SAR data: the P-SBAS service within the ESA G-POD environment. *Remote Sens*., **7,** 15630–15650.

De Michele, M. & Briole, P.: 2007 Deformation between 1989 and 1997 at Piton de la Fournaise volcano retrieved from correlation of panchromatic airborne images, *Geophys. J.. Int,* **169,** 357–364.

De Novellis, V. *et al.* 2019 DInSAR analysis and analytical modeling of Mount Etna displacements: the December 2018 volcano-tectonic crisis, *Geophys. Res. Lett.,* **46**(11), 5817–5827.

ESA, 2015. Geohazards-Thematic Exploitation Platform [WWW Document]. URL https://geohazards-tep.eu(accessed 10.2.20).

Faccenna, C. *et al.* 2011. Topography of the Calabria subduction zone (southern Italy): clues for the origin of Mt. *Etna. Tectonics,* **30**. https://doi.org/10.1029/2010TC002694.

Firth, C., Stewart, I., Mcguire, W.J., Kershaw, S. & Vita-Finzi, C., 1996. Coastal elevation changes in eastern Sicily: implications for volcano instability at Mount Etna. *Geol. Soc. Spec. Publ.,* **110,** 153–167.

Froger, J.L., Merle, O. & Briole, P., 2001. Active spreading and regional extension at Mount Etna imaged by SAR interferometry. *Earth planet. Sci. Lett.,* **187,** 245–258.

Goes, S., Jenny, S., Hollenstein, C., Kahle, H.G. & Geiger, A., 2004. A recent tectonic reorganization in the south-central Mediterranean. *Earth planet. Sci. Lett.,* **226,** 335–345.

Goldstein, R. M. & Werner, C. L.: 1998 Radar interferogram filtering for geophysical applications, *Geophys. Res. Lett.,* **25**(21), 4035–4038.

Hirn, A. *et al.* 1997. Roots of Etna volcano in faults of great earthquakes. *Earth Planet. Sci. Lett.,* **148,** 171–191.

Huang, M.-H. *et al.* 2006 A growing structure near the deformation front in SW Taiwan as deduced from SAR interferometry and geodetic observation, *Geophys. Res. Lett.,* **33**(12), L12305, doi:10.1029/2005GL025613.

Imposa, S., De Guidi, G., Grassi, S., Scudero, S., Barreca, G., Patti, G. & Boso, D.: 2015 Applying geophysical techniques to investigate a segment of a creeping fault in the urban area of San Gregorio di Catania, southern flank of Mt. Etna (Sicily - Italy), *J. appl. Geophys.,* **123,** 153–163.

INGV RING Working Group, 2016. *Rete Integrata Nazionale GNSS,* http://ring.gm.ingv.it.

Kershaw, S., 2000. Quaternary reefs of Northeastern Sicily: structure and growth controls in an unstable tectonic setting. *J. Coast. Res.,* **16,** 1037–1062.

Labaume, P., Claude Bousquet, J. & Lanzafame, G., 1990. Early deformations at a submarine compressive front: the quaternary Catania foredeep south of Mt. Etna, Sicily, Italy. *Tectonophysics,* **177,** 349–366.

Lo Giudice, E. & Rasà, R., 1992. Very shallow earthquakes and brittle deformation in active volcanic areas: the Eatnean region as an example. *Tectonophysics,* **202,** 257–268.

Manunta, M. *et al.* 2019. The parallel SBAS approach for Sentinel-1 interferometric wide swath deformation time-series generation: algorithm description and products quality assessment. *IEEE Trans. Geosci. Remote Sens.,* **57,** 6259–6281.

Mattia, M. *et al.* 2015. A comprehensive interpretative model of slow slip events on Mt. Etna's eastern flank. *Geochem. Geophys. Geosyst.,* **16,** 635–658.

Mattia, M., Bruno, V., Montgomery-Brown, E., Patanè, D., Barberi, G. & Coltelli, M.: 2020 Combined seismic and geodetic analysis before, during, and after the 2018 Mount Etna Eruption, *Geochem. Geophys. Geosyst.,* **21**(9), 1–16.

Monaco, C. *et al.* 2021 The seismogenic source of the 2018 December 26th earthquake (Mt. Etna, Italy): a shear zone in the unstable eastern flank of the volcano, *J. Geodyn.,* **143,** 101807, doi:10.1016/j.jog.2020.101807.

Monaco, C., Tapponnier, P., Tortorici, L. & Gillot, P.Y., 1997. Late Quaternary slip rates on the Acireale-Piedimonte normal faults and tectonic origin of Mt. Etna (Sicily). *Earth Planet. Sci. Lett.,* **147,** 125–139.

Monaco, C. & Tortorici, L., 2000. Active faulting in the Calabrian arc and eastern Sicily. *J. Geodyn.,* **29,** 407–424.

Nishimura, T., Tobita, M., Yarai, H., Amagai, T., Fujiwara, M., Une, H. & Koarai, M.: 2008 Episodic growth of fault-related fold in northern Japan observed by SAR interferometry, *Geophys. Res. Lett.,* **35**(13), L13301, doi:10.1029/2008GL034337.

Palano, M., 2016. Episodic slow slip events and seaward flank motion at Mt. Etna volcano (Italy). *J. Volc. Geotherm. Res.,* **324,** 8–14.

Palano, M. *et al.* 2012. GPS velocity and strain fields in Sicily and southern Calabria, Italy: updated geodetic constraints on tectonic block interaction

in the central Mediterranean. *J. geophys. Res. Solid Earth,* **117,** https://doi.org/10.1029/2012JB009254.

Palano, M., Sparacino, F., Gambino, P., D'Agostino, N. & Calcaterra, S. (2022) Slow slip events and flank instability at Mt. Etna volcano (Italy). *Tectonophysics,* **836,** 229414, doi:10.1016/J.TECTO.2022.229414.

Pepe, A., Yang, Y., Manzo, M. & Lanari, R.(2015). Improved EMCF-SBAS processing chain based on advanced techniques for the noise-filtering and selection of small baseline multi-look DInSAR interferograms. *IEEE Trans. Geosci. Remote Sens.,* **53**(8), 4394–4417.

Poland, M. P., Peltier, A., Bonforte, A. & Puglisi, G.: 2017 The spectrum of persistent volcanic flank instability: a review and proposed framework based on Kīlauea, Piton de la Fournaise, and Etna, *J. Volc. Geotherm. Res.,* **339,** 63–80.

Rasà, R., Azzaro, R. & Leonardi, O., 1996. Aseismic creep on faults and flank instability at Mount Etna volcano, *Sicily. Geol. Soc. Spec. Publ.,* **110,** 179–192.

Regione Siciliana, 2010. Modello digitale del terreno (MDT) 2 m x 2 m Regione Siciliana-ATA 2007-2008 [WWW Document]. URL. http://www.sitr.regione.sicilia.it

Ristuccia, G.M., Di Stefano, A., Gueli, A.M., Monaco, C., Stella, G. & Troja, S.O., 2013. OSL chronology of quaternary terraced deposits outcropping between Mt. Etna volcano and the Catania Plain (Sicily, southern Italy). *Phys. Chem. Earth,* **63,** 36–46.

Rust, D. & Kershaw, S., 2000. Holocene tectonic uplift patterns in northeastern Sicily: evidence from marine notches in coastal outcrops. *Mar. Geol.,* **167,** 105–126.

Schellart, W.P.P., 2010. Mount Etna–Iblean volcanism caused by rollback-induced upper mantle upwelling around the Ionian slab edge: an alternative to the plume model. *Geology,* **38,** 691–694.

Solaro, G., Acocella, V., Pepe, S., Ruch, J., Neri, M. & Sansosti, E., 2010. Anatomy of an unstable volcano from InSAR: multiple processes affecting flank instability at Mt. Etna, 1994-2008. *J. geophys. Res. Solid Earth,* **115,** 1994–2008.

Spampinato, C.R., Scicchitano, G., Ferranti, L. & Monaco, C., 2012. Raised Holocene paleo-shorelines along the Capo Schisò coast, Taormina: new evidence of recent co-seismic deformation in northeastern Sicily (Italy). *J. Geodyn.,* **55,** 18–31.

Stewart, I.S., Cundy, A., Kershaw, S. & Firth, C., 1997. Holocene coastal uplift in the taormina area, northeastern sicily: implications for the southern prolongation of the calabrian seismogenic belt. *J. Geodyn.,* **24,** 37–50.

Tortorici, L., Monaco, C., Tansi, C. & Cocina, O., 1995. Recent and active tectonics in the Calabrian arc (Southern Italy). *Tectonophysics,* **243,** 37–55.

Tringali, G. *et al.* 2022. Fault rupture and aseismic creep accompanying the December 26, 2018, Mw 4.9 Fleri earthquake (Mt. Etna, Italy): factors affecting the surface faulting in a volcano-tectonic environment. *Quat. Int.* **651,** 25–41, https://doi.org/10.1016/j.quaint.2021.12.019.

Urlaub, M. *et al.* 2018 Gravitational collapse of Mount Etna's southeastern flank, *Sci. Adv.,* **4,** 1–8.

Walsh, J.J., Nicol, A. & Childs, C., 2002. An alternative model for the growth of faults. *J. Struct. Geol.,* **24,** 1669–1675.

Westaway, R., 1993. Quaternary uplift of southern Italy. *J. geophys. Res.,* **98,** 21741–21772.

SUPPORTING INFORMATION

Supplementary data are available at *GJI* online.

S1_Time Series of GNSS campaign Points INGV-OE.docx
S2_Time Series of GNSS campaign Points UNICT-Net.docx
S3_Faults_Offset.docx
S4_Permanent Scatters.docx
S5_Location PS of Fig 8 Fig 11 and Fig 12.docx
S6_earthquakes_2016_2019.xlsx
S7_Time_series_EBDA_ETEC_PSs_2019.xlsx

Please note: Oxford University Press is not responsible for the content or functionality of any supporting materials supplied by the authors. Any queries (other than missing material) should be directed to the corresponding author for the paper.